J. Fluid Mech. (1996), vol. 328, pp. 177–227

Simulations of the viscous flow normal to an impulsively started and uniformly accelerated flat plate

By P. KOUMOUTSAKOS[1] AND D. SHIELS[2]

[1]Center for Turbulence Research, NASA Ames 202A-1, Moffett Field, 94035 CA, USA

[2]Graduate Aeronautical Laboratories, California Institute of Technology, Pasadena, 91125 CA, USA

(Received 21 October 1994 and in revised form 17 July 1996)

The development of a two-dimensional viscous incompressible flow generated from an infinitesimally thin flat plate, impulsively started or uniformly accelerated normal to the free stream is studied computationally. An adaptive numerical scheme, based on vortex methods, is used to integrate the vorticity–velocity formulation of the Navier–Stokes equations. The results of the computations complement relevant experimental works while providing us with quantities such as the vorticity field and the unsteady forces experienced by the body. For the uniformly accelerated plate the present simulations capture the development of a number of centers of vorticity along the primary separating shear layer. This phenomenon has been observed in experimental works but has not been predicted by inviscid models. The present simulations suggest that this Kelvin–Helmholtz-type instability is driven by the interaction of primary and secondary vorticity near the tips of the plate and depends on the acceleration of the plate.

1. Introduction

The flow past a thin flat plate normal to the free stream is a classic example of bluff body flows. The formation of vortices at the sharp edges is of fundamental importance to the study of vortex generation and the development of separating shear layers. Prandtl (1904) was the first to study experimentally the flow behind a flat plate moving normal to itself. Later experimental studies of the phenomenon were presented by Anton (1939) and Wedemeyer (1956). Pierce (1961) employed spark shadowgraph techniques to produce the well-known photographic evidence of separation at sharp edges. Taneda & Honji (1971) used the aluminium dust method to provide visualizations of the flow past impulsively started and uniformly accelerated flat plates. On a similar note Pullin & Perry (1980) used dye in water to study the development of the separating shear layers past thin wedges. Lian & Huang (1989) used the hydrogen bubble technique to provide visualizations of the flow past accelerating plates. A more recent experimental investigation was presented by Coutanceau and Launay (in Dennis *et al.* 1993) for the impulsively started plate at moderate Reynolds numbers. They present extensive results for the early time development of the wake and they discuss the effect of blockage ratio in their experiments.

Unlike other bluff body flows, the separation points for the flat plate are identified

with the edges of the pate. This simplification has attracted the interest of several theoretical studies. By appropriately estimating the production of circulation at the tips of the plate and assuming an otherwise inviscid evolution of the vorticity field, several investigators have presented analytical calculations for this type of flow (Villat 1930; Wedemeyer 1961; Pullin 1978; Krasny 1991).

Numerical simulations of the viscous flow past a flat plate are hindered by the presence of singularities of the Navier–Stokes equations at the tips of the plate. Past computations on this flow (Sarpkaya 1975; Chua 1990) relied on estimating the production of circulation at the tips of the plate and subsequently shedding discrete vortices from the plate edges that are allowed to evolve and form a wake. Alternatively, fractional step Taylor–Galerkin (Laval & Quartapelle 1990; Tamaddon-Jahromi, Townsend & Webster 1994) and high-order finite difference (Najjar & Vanka 1995) methods have been employed to solve the Navier–Stokes equations. These investigations deal mostly with long-time behaviour of the flow and global quantities such as Strouhal frequency and streamlines. Najjar & Vanka (1995) provide additional information for a wide range of Reynolds numbers such as the vorticity field and forces experienced by the body as well as discussion of the effect of three-dimensionality in such flows. These simulations employ grids that are refined near the surface of the plate, but do not explicitly handle the singularity at the tips of the plate.

On the other hand rigorous numerical schemes have been developed for the study of the steady state of the flow that is realized at low and moderate Reynolds numbers. Smith (1979) was the first to develop a numerical scheme which avoids the plate-tip singularity and presented steady-state results for low Reynolds numbers. Ingham, Tang & Morton (1991, referred to as ITM from here on) used an analytic solution to match the singularities at the plate edges and a second-order finite difference scheme to solve the vorticity/streamfunction formulation of the Navier–Stokes equations while handling the upstream and downstream boundary conditions with a method suggested by Fornberg (1980). Dennis *et al.* (1993) implemented a formulation in primitive variables that is not directly affected by the presence of the singularity, and presented an extensive study of the steady state of this flow. More recently In, Choi & Kim (1995) developed a procedure, similar to that employed by ITM, that treats the singularity at the tips of the plate analytically and then matches it to an outer finite difference solution. They used their methodology to conduct simulations for various angles of attack and for Reynolds numbers up to 30. Note that there seems to be a discrepancy among the reported results of the steady-state computations, with differences of up to 20% in estimating the length of the recirculating bubble. These differences may be attributed to the treatment of the boundary and far-field conditions by the various schemes described above.

In the present work we conduct high-resolution simulations of the early time development of the wake behind a flat plate impulsively started or uniformly accelerated normal to the flow. Our scheme is based on the classical scheme of vortex methods (Chorin 1973; Leonard 1980), enhanced to account accurately for viscous effects (diffusion and no-slip boundary condition) and the singularities at the tips of the plate. The efficient implementation of the scheme of multipole expansions (Greengard & Rohklin 1987) allows us to implement large numbers of vortex elements (of the $O(10^6)$) to resolve a wide range of scales in the flows under consideration. The present results complement and extend the experimental work of Dennis *et al.* (1993) on the impulsively started flow. For the viscous flow past a uniformly accelerating flat plate, to the authors best knowledge, the present results are the first to verify computationally the formation of centres of vorticity along the primary separating shear layer. In

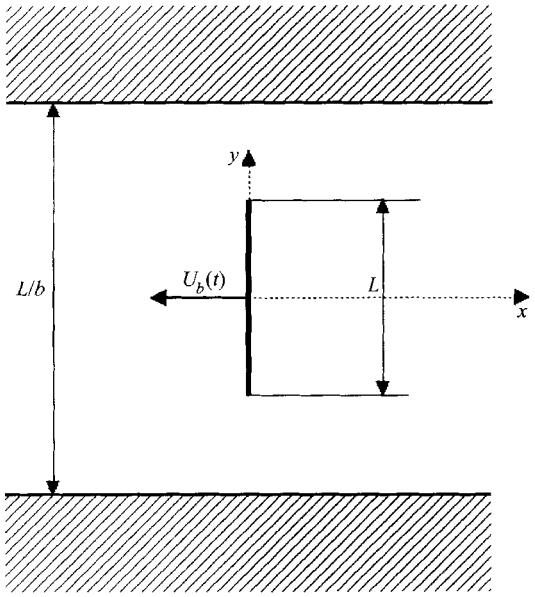

FIGURE 1. Definition sketch.

an effort to clarify the discrepancies between past experimental results and theoretical investigations concerning the onset of an instability along the separating shear layers, we conduct a series of simulations and present a detailed description of the flow. We discuss the mechanism of formation of discrete vortices along the separating shear layer in terms of quantities such as the vorticity field that are difficult to obtain experimentally. Furthermore the results of the present simulations reveal similarity laws obeyed by the global quantities of the flow, such as the wake length and the drag coefficient, for the uniformly accelerated flow past a flat plate.

2. The two-dimensional Navier–Stokes equations

Two-dimensional incompressible unsteady flow of a viscous fluid may be determined by the vorticity transport equation as

$$\frac{\partial \omega}{\partial t} + \boldsymbol{u} \cdot \nabla \omega = \nu \nabla^2 \omega \tag{1}$$

where $\boldsymbol{u}(\boldsymbol{x}, t)$ is the velocity, $\boldsymbol{\omega} = \omega \hat{e}_z = \nabla \times \boldsymbol{u}$ the vorticity and ν denotes the kinematic viscosity. For flow around a flat plate, translating with velocity $\boldsymbol{U}_b(t)$ (figure 1) the velocity of the fluid ($\boldsymbol{u}$) on the surface of the body ($\boldsymbol{x}_s$) is equal to the velocity of the body :

$$\boldsymbol{u}(\boldsymbol{x}_s, t) = \boldsymbol{U}_b(t) \tag{1a}$$

At infinity we have

$$\boldsymbol{u}(\boldsymbol{x}) \to \boldsymbol{U}_\infty \qquad \text{as} \quad |\boldsymbol{x}| \to \infty \tag{1b}$$

where $\boldsymbol{U}_\infty$ is the free-stream velocity. Using the definition of the vorticity and the continuity ($\nabla \cdot \boldsymbol{u} = 0$) it can be shown that $\boldsymbol{u}$ is related to $\boldsymbol{\omega}$ by the following Poisson equation:

$$\nabla^2 \boldsymbol{u} = -\nabla \times \boldsymbol{\omega}. \tag{2}$$

The velocity–vorticity formulation helps in eliminating the pressure from the unknowns of the equations. However, for bounded domains it introduces additional constraints in the kinematics of the flow field and requires the transformation of the velocity boundary conditions to vorticity form.

2.1. *Particle (vortex) methods*

The present numerical method is based on the discretization of the above equations in a Lagrangian frame using particle (vortex) methods. The vorticity equation (1) may be expressed in a Lagrangian formulation by solving for vorticity-carrying fluid elements ($\boldsymbol{x}_a$) based on the following set of equations:

$$\frac{\mathrm{d}\boldsymbol{x}_a}{\mathrm{d}t} = \boldsymbol{u}(\boldsymbol{x}_a, t), \quad \frac{\mathrm{d}\omega}{\mathrm{d}t} = \nu \nabla^2 \omega. \tag{3}$$

In order to enforce the boundary conditions a fractional step algorithm is implemented. This algorithm is described in §4.

In the context of particle methods it is desirable to replace the right-hand side of (3) by integral operators. These operators are discretized using the locations of the particles as quadrature points so that ultimately (3) is replaced by a set of ODEs whose solution is equivalent to the solution of the original set of equations. To this effect the velocity field may be determined by the vorticity field using the Green's function formulation for the solution of Poisson's equation (2).

$$\boldsymbol{u} = -\frac{1}{2\pi} \int \boldsymbol{K}(\boldsymbol{x} - \boldsymbol{y}) \times \boldsymbol{\omega} \, \mathrm{d}\boldsymbol{y} + \boldsymbol{U}_0(\boldsymbol{x}, t) \tag{4}$$

where $\boldsymbol{U}_0(\boldsymbol{x}, t)$ is the solution of the homogeneous equation with the no-through-flow boundary condition enforced , and $\boldsymbol{K}(z) = z/|z|^2$. The use of the Biot-Savart law to compute the velocity field guarantees the enforcement of the boundary condition at infinity.

For the diffusion equation, the Laplacian operator may be approximated by an integral operator (Degond & Mas-Gallic 1989) as well so that

$$\nabla^2 \omega \approx \int G(|\boldsymbol{x} - \boldsymbol{y}|) \, [\omega(\boldsymbol{x}) - \omega(\boldsymbol{y})] \, \mathrm{d}\boldsymbol{y} \tag{5}$$

where, in this paper, G is taken to be the Green's function kernel for the diffusion equation in an unbounded domain. The boundary condition (1*a*) is enforced by formulating the physical mechanism which it describes. The surface of the plate is the source of vorticity that enters the flow. A vorticity flux ($\partial\omega/\partial n$) may be determined on the boundary in a way that ensures (1*a*) is satisfied (Koumoutsakos, Leonard & Pépin 1994*a*, referred to as KLP hereinafter). We implement a fractional step algorithm that allows for the calculation of this vorticity flux and its diffusive distribution into the flow via an integral operator. We replace then, the right-hand side of (3) with the following set of equations:

$$\left.\begin{aligned} \frac{\mathrm{d}\boldsymbol{x}_a}{\mathrm{d}t} &= -\frac{1}{2\pi} \int \boldsymbol{K}(\boldsymbol{x}_a - \boldsymbol{y}) \times \boldsymbol{\omega} \, \mathrm{d}\boldsymbol{y} + \boldsymbol{U}_0(\boldsymbol{x}_a, t), \\ \frac{\mathrm{d}\omega}{\mathrm{d}t} &\approx \nu \int G(|\boldsymbol{x}_a - \boldsymbol{y}|) \, [\omega(\boldsymbol{x}_a) - \omega(\boldsymbol{y})] \, \mathrm{d}\boldsymbol{y} + \nu \int H(\boldsymbol{x}_a, \boldsymbol{y}) \, \frac{\partial \omega}{\partial n}(\boldsymbol{y}) \, \mathrm{d}\boldsymbol{y}, \end{aligned}\right\} \tag{6}$$

where the kernel H is developed in KLP. In vortex methods, the vorticity field is considered as a discrete sum of the individual vorticity fields of the particles, having core radius ϵ, strength $\Gamma(t)$ and an individual distribution of vorticity determined by

the function η_ϵ so that

$$\omega(\boldsymbol{x},t) = \sum_{n=1}^{N(t)} \Gamma_n(t)\, \eta_\epsilon(\boldsymbol{x} - \boldsymbol{x}_n(t)). \tag{7}$$

When this expression for the vorticity is substituted in (6) the singular integral operators K, G are convolved with the smooth function η_ϵ and are replaced by smooth operators K_ϵ, G_ϵ. In the present study the Gaussian smoothing was used:

$$\eta_\epsilon(\boldsymbol{x}) = \frac{1}{2\pi\epsilon^2}\, \mathrm{e}^{-|\boldsymbol{x}|/2\pi\epsilon^2}$$

and the respective forms of K_ϵ and G_ϵ are given by

$$\boldsymbol{K}_\epsilon(\boldsymbol{x}) = \frac{1}{2\,\epsilon^2}\frac{\boldsymbol{x}}{|\boldsymbol{x}|^2}(1 - \mathrm{e}^{-|\boldsymbol{x}|^2/2\epsilon^2}), \quad G_\epsilon(|\boldsymbol{x}|) = \frac{1}{2\,\pi\epsilon^2}\, \mathrm{e}^{-|\boldsymbol{x}|^2/2\epsilon^2}. \tag{8}$$

The error in vortex methods may be described as a combination of the errors made by the smoothing of the Biot-Savart and the diffusion kernel and the discretization on the location of the particles via a quadrature rule. The error in the vorticity field induced by the approximation of the convection is expressed as

$$\text{Smoothing error} + \text{Discretization error} = O(\epsilon^m) + O(h^n/\epsilon^n) \tag{9}$$

and by the diffusion (Degond & Mas-Gallic 1989) as

$$\text{Smoothing error} + \text{Discretization error} = O(\epsilon^m) + O(h^n/\epsilon^{n+1}) \tag{10}$$

where h is a characteristic distance between the particles and the coefficients m and n depend on the properties of the smoothing function η_ϵ (for the Gaussian $m = 2$ and $n = \infty$). The convergence properties of the method require that the particles overlap ($h/\epsilon < 1$) at all times. The theoretical estimates (10) and practice dictate that this constraint is even more necessary due to the approximation of the diffusion by the scheme of Particle Strength Exchange.

The integrals are discretized using a quadrature having as quadrature points the locations of the particles. Assuming that each particle occupies a region of area h^2 and that the shape of the body is discretized by M panels then algorithmically the method may be expressed as:

$$\left.\begin{aligned} &\frac{\mathrm{d}\boldsymbol{x}_i}{\mathrm{d}t} = -\frac{1}{2\pi}\sum_{j=1}^{N(t)} \Gamma_j\, \boldsymbol{K}_\epsilon(\boldsymbol{x}_i - \boldsymbol{x}_j) + \boldsymbol{U}_0(\boldsymbol{x}_i, t), \\ &\frac{\mathrm{d}\Gamma_i}{\mathrm{d}t} = \nu \sum_{j=1}^{N(t)} [\Gamma_j - \Gamma_i]\, G_\epsilon(|\boldsymbol{x}_i - \boldsymbol{x}_j|) + \nu \sum_{m=1}^{M} H(\boldsymbol{x}_i, \boldsymbol{x}_m)\, \frac{\partial\omega}{\partial n}(\boldsymbol{x}_m), \\ &\Gamma_i(0) = \omega(\boldsymbol{x}_i, 0)\, h^2, \qquad i = 1, 2, \ldots, N(t). \end{aligned}\right\} \tag{11}$$

The Lagrangian representation of the convective terms avoids many difficulties associated with its discretization on an Eulerian mesh such as excess numerical diffusion. However, the straightforward method of computing the right-hand side of (11) for every particle requires $O(N^2)$ operations for N vortex elements. This is an N-body type of problem which appears in several fields of engineering and science. In order to reduce this cost Barnes & Hut (1986) presented an algorithm for gravitational interactions that has an operation count of $O(N\log N)$. Greengard & Rohklin (1987)

presented an alternative scheme, applicable to a variety of problems involving integral equations, with computational cost of $O(N)$. In the present scheme the efficient vectorization (Koumoutsakos 1996) of the $O(N)$ scheme allows computations with one CPU min per velocity evaluation for one million vortices on a single processor of a CRAY YMP.

Note that in the present method the number of particles (N) used in the simulations is a function of time, as the particles adapt to resolve the vorticity field that is generated around the surface of the plate and is subsequently convected and diffused. New computational elements are added as needed using the remeshing procedure discussed in §3.

3. Remeshing

The accuracy of the present method relies on the accuracy of the quadrature rule as information needs to be gathered from the possibly distorted (due to the strain of the flow field) particle positions. A key aspect of the present algorithm is the implementation of a remeshing procedure to ensure the regularity (i.e. overlap) of the Lagrangian computational elements. This regularity is not only necessary for the accuracy of the quadrature approximation of the integrals but furthermore it is dictated by the numerical approximation of the viscous effects in the present scheme. More specifically, the scheme of PSE requires that a set of zero-strength particles always surrounds the vortical regions of the flow to properly approximate the diffusion process. The enforcement of the no-slip boundary condition via the diffusive distribution of the vorticity flux from the surface of the plate requires that computational elements are always surrounding the surface of the body in order to perform an accurate quadrature of the related integral operator. As the computational elements in vortex methods are inherently linked to the vorticity field, they have to adapt as the vorticity field is convected and diffused. The remeshing procedure guarantees that the particles overlap at all locations of the domain. It ensures that the area surrounding the surface of the plate is not depleted of particles and that 'ghost' particles always surround the regions of vorticity to properly account for diffusion.

In order to remesh on the distorted Lagrangian grid (particles) we overlay a uniform rectangular grid. It is necessary to accurately interpolate the old vorticity field (ω) onto the new grid initially equi-spaced particle locations ($\tilde{x}$) – that replace the (distorted) particle locations (x). After remeshing, the equi-spaced rectangular grid cell centres become the new particle locations. The new particle strengths are determined using an appropriate interpolation kernel Λ so that:

$$\tilde{\Gamma}_i(\tilde{x}_i) \approx \sum_{j=1}^{M} \Gamma_j(x_j)\, \Lambda(\tilde{x}_i - x_j), \tag{12}$$

where $\tilde{\Gamma}, \Gamma$ denote the new and old particle strengths respectively.

Depending on the order (k) of the interpolation we may write that

$$\tilde{\omega}(\tilde{x}) = \omega(x) + O(h^k). \tag{13}$$

The process is not of the usual interpolation type as it is complicated by the fact that the particles are disordered. The basic analysis of interpolation of this type is given by Schoenberg (1973). He has developed interpolation formulas that attempt to minimize the effect of the grid disorder on the interpolated quantity. If h is the spacing of the new grid setting $u = |x|/h$ then interpolation kernels of this type are:

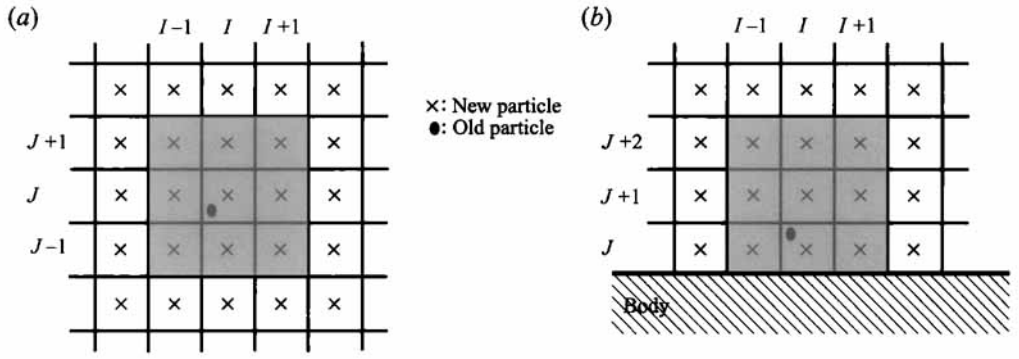

FIGURE 2. Remeshing (*a*) in the unbounded domain, (*b*) near the surface of the plate.

zeroth-order interpolation

$$\Lambda_0(u) = \begin{cases} 1 & \text{if } 0 \leqslant u \leqslant 1/2 \\ 0 & \text{otherwise,} \end{cases} \tag{14}$$

which is the nearest grid point (NGP) interpolation

linear interpolation

$$\Lambda_1(u) = \begin{cases} 1-u & \text{if } 0 \leqslant u \leqslant 1 \\ 0 & \text{otherwise,} \end{cases} \tag{15}$$

which is usually the choice in Cloud in Cell schemes;

second-order interpolation

$$\Lambda_2(u) = \begin{cases} 1-u^2 & \text{if } 0 \leqslant u < 1/2 \\ (1-u)(2-u)/2 & \text{if } 1/2 \leqslant u < 3/2 \\ 0 & \text{otherwise;} \end{cases} \tag{16}$$

Everett's formula of third order

$$\Lambda_3(u) = \begin{cases} (1-u^2)(2-u)/2 & \text{if } 0 \leqslant u < 1 \\ (1-u)(2-u)(3-u)/6 & \text{if } 1 \leqslant u < 2 \\ 0 & \text{otherwise.} \end{cases} \tag{17}$$

In our algorithm we use $\Lambda_2(u)$ to perform this remeshing, conserving the circulation and the linear and angular momentum of the vorticity field. The two-dimensional remeshing formulas are Cartesian products of their one-dimensional counterparts. The interpolation kernel is defined then as

$$\Lambda(x, y) = \Lambda(x)\Lambda(y). \tag{18}$$

Using Λ_2, each particle located in a cell (I, J) affects 9 mesh points, presented as shaded areas in figure 2(*a*). The *frequency* of remeshing depends on the strain field of the particular flow field. In the present study the frequency of remeshing was variable throughout the course of the simulations, depending on the conservation of the moments of the vorticity field. Simulations were also carried out with a fixed remeshing frequency whose value was decided empirically. A convergence study in §5 described the effect of remeshing on the results of the simulations.

3.1. *Remeshing in a bounded domain*

When boundaries are present the remeshing procedure is complicated as the new mesh-points have to be outside the body. It is evident then that the schemes employed

for an unbounded domain have to be modified for particles that are located in an (I,J) cell which is adjacent to the boundary. Here we devise a scheme to overcome this difficulty. It requires again 9 points and conserves the same quantities as for the unbounded case. In figure 2(*b*) the nine cells affected by a cell adjacent to the boundary are depicted. The interpolating kernel is again the product of two one-dimensional forms but now

$$\Lambda(x,y) = \Lambda_I(x)\Lambda_J(y) \tag{19}$$

with $\Lambda_I = \Lambda_2$ and

$$\Lambda_J = \begin{cases} 1 - 3/2\, v + 1/2\, v^2 & \text{for cells } J \\ v\,(2-v) & \text{for cells } J+1 \\ v\,(v-1)/2 & \text{for cells } J+2 \\ 0 & \text{for all other } I \end{cases} \tag{20}$$

where $v = (y - y')/h$ and J denotes the off-boundary direction.

4. Boundary conditions

The no-slip boundary condition accounts for the generation of vorticity on the surface of the body. The surface of the body acts as a source of vorticity (Lighthill 1963; Schmall & Kinney 1974) and the task is to relate this vorticity flux on the surface of the body to the no-slip condition. This process is described in KLP for non-zero-thickness bodies and has been implemented in the simulation of the flow past an impulsively started cylinder (Koumoutsakos & Leonard 1995). Here we extend this technique to the case of a zero-thickness flat plate by properly relating the kinematic and dynamic constraints of the flow.

4.1. *A fractional step algorithm*

In the present formulation, (11) are not integrated simultaneously in time but instead a fractional step algorithm is employed. We solve successively for the convective and for the viscous part of the equations and at each substep we enforce the relevant kinematic (no-through-flow) and dynamic (no-slip) boundary conditions.

To illustrate our computational scheme, let us assume that at the nth time step (corresponding to time $t - \delta t$) the vorticity field has been computed and we seek to advance the solution to the next time step (time t). The following two-step procedure is implemented:

Step 1: Convection

Using as initial conditions the vorticity field at $t - \delta t$ ($\omega^n(\boldsymbol{x}^n, n\delta t)$) we need to solve for

$$\frac{\partial \omega}{\partial t} + \boldsymbol{u} \cdot \nabla \omega = 0. \tag{20a}$$

This set of equations is complemented with the no-through flow boundary condition

$$\boldsymbol{u}(\boldsymbol{x}_s, t) \cdot \boldsymbol{n} = \boldsymbol{U}_b(t) \cdot \boldsymbol{n} \tag{20b}$$

where $\boldsymbol{n}$ denotes the normal on the surface of the plate. Without loss of generality we assume that the plate surface lies along the y-axis at $x = 0$ and between $-L/2 \leqslant y \leqslant L/2$. In order to enforce the no-through-flow boundary condition a vortex sheet of strength κ is distributed on the plate surface. The strength of this vortex sheet is

then determined by the solution of the following integral equation:

$$-\frac{1}{2\pi}\int_{-L/2}^{L/2}\frac{\kappa(\xi)}{y-\xi}\mathrm{d}\xi = u_n(y) = \boldsymbol{u}(y\hat{\boldsymbol{e}}_y, t)\cdot\hat{\boldsymbol{e}}_x \tag{21a}$$

where $u_n(y)$ is the velocity normal to the surface of the plate. The above integral equation is singular as it admits more than one solution. A unique solution is obtained by enforcing the conservation of circulation (note that in airfoil theory κ is uniquely determined by enforcing the Kutta condition)

$$\int_{-L/2}^{L/2}\kappa(\xi)\mathrm{d}\xi = -\int\omega(\boldsymbol{x}, n\,\delta t)\mathrm{d}\boldsymbol{x} = -\Gamma \tag{21b}$$

where Γ is the total circulation in the wake. For the symmetric flows examined herein Γ is nominally zero.

In order to solve the set of equations (21) we introduce the transformation $\cos(\theta) = -2y/L$ and use the orthogonality of a Fourier series expansion for $\kappa(\theta)$ over the interval $[0, \pi]$ (Batchelor 1967) to obtain that at each instant of time

$$\kappa(\theta) = -A_0\frac{\cos\theta}{\sin\theta} + \frac{C}{\sin\theta} + 2\sum_{m=1}^{\infty}A_m\sin(m\theta) \tag{22a}$$

where

$$A_m = \frac{2}{\pi}\int_0^{\pi}u_n(\theta)\cos(m\theta)\mathrm{d}\theta \qquad \text{for} \quad m = 0, 1, \ldots, \infty \tag{22b}$$

and C is determined by enforcing the conservation of circulation (21*b*):

$$C = \frac{2\Gamma}{\pi L} + A_1. \tag{22c}$$

A finite number of terms (P) is retained in the infinite series (22*a*) in the numerical implementation of this method. Note that the above expression for $\kappa(\theta)$ has the singularity of the vortex sheet at the tips of the plate built-in.

The velocity field at the locations of the particles ($\boldsymbol{u}(\boldsymbol{x}_i)$) is then calculated as

$$\boldsymbol{u}(\boldsymbol{x}_i, n\delta t) = -\frac{1}{2\pi}\int\boldsymbol{K}(\boldsymbol{x}_i - \boldsymbol{y})\times\boldsymbol{\omega}(\boldsymbol{y}, n\delta t)\,\mathrm{d}\boldsymbol{y} + \frac{1}{2\pi}\int_{-L/2}^{L/2}\frac{\kappa(\boldsymbol{\xi}, n\delta t)}{\boldsymbol{x}_i - \boldsymbol{\xi}}\mathrm{d}\boldsymbol{\xi} \tag{23}$$

where $\boldsymbol{\xi} = \xi\,\hat{\boldsymbol{e}}_y$.

Algorithmically Step 1 may be expressed as

$$\frac{\mathrm{d}\boldsymbol{x}_i}{\mathrm{d}t} = \boldsymbol{u}(\boldsymbol{x}_i, n\delta t), \quad \frac{\mathrm{d}\Gamma_i}{\mathrm{d}t} = 0 \tag{24}$$

for $i = 1 \ldots, N(n\,\delta t)$.

In order to numerically integrate (24) we use an Adams–Bashforth scheme of order 2. As in the following sub-step, the viscous effects are accounted for, by modifying the strength of the particles without modifying their locations (as is the case in the method of random walk (Chorin 1973)) we have

$$\boldsymbol{x}_i^{n+1} = \boldsymbol{x}_i^n + \tfrac{3}{2}\big(2\,\boldsymbol{u}(\boldsymbol{x}_i^n, n\delta t) - \boldsymbol{u}(\boldsymbol{x}_i^n, (n-1)\delta t)\big). \tag{25}$$

At the end of Step 1 a vorticity field $\omega' = \omega(\boldsymbol{x}, (n + 1/2)\delta t)$ has been established in the flow field.

Step 2: Diffusion and vorticity creation

In this stage we solve for the viscous part of the equations and the boundary conditions. Using as initial conditions the vorticity field established at the previous sub-step we solve

$$\frac{\mathrm{d}\omega}{\mathrm{d}t} = \nu \nabla^2 \omega \tag{26a}$$

while enforcing the no-slip boundary condition

$$\boldsymbol{u}(\boldsymbol{x}_s, t) \cdot \boldsymbol{s} = \boldsymbol{U}_b(t) \cdot \boldsymbol{s} \tag{26b}$$

by appropriately determining a vorticity flux ($\partial\omega/\partial n$) and hence a Neuman-type boundary condition for the vorticity field on the surface of the plate.

First, in order to solve for the diffusion of the vorticity field we employ the scheme of Particle Strength Exchange (Degond & Mas-Gallic 1989). In this scheme the diffusion operator is approximated by an integral operator that, when discretized using as quadrature points the locations of the particles, amounts to the exchange of circulations of the individual vortex blobs according to

$$\frac{\mathrm{d}\Gamma_i}{\mathrm{d}t} = \frac{\nu h^2}{\epsilon^2} \sum_{j=1}^{N(t)} [\Gamma_j^n - \Gamma_i^n]\, G_\epsilon(|\boldsymbol{x}_i^{n+1} - \boldsymbol{x}_j^{n+1}|). \tag{27}$$

When Gaussian vortex blobs are implemented it has been observed (Koumoutsakos 1993) that optimum results are obtained with an Euler-type integration scheme with time step $\delta t = \epsilon^2/2\nu$ so that the particle strengths are updated according to

$$\Gamma_i^{n+1/2} = \Gamma_i^n + \frac{h^2}{4\pi\epsilon^2} \sum_{j=1}^{N(t)} (\Gamma_j^n - \Gamma_i^n)\, \mathrm{e}^{-|\boldsymbol{x}_i^{n+1} - \boldsymbol{x}_j^{n+1}|^2/2\epsilon^2}. \tag{28}$$

Once the particle strengths and locations have been updated (28) and (25), respectively, a tangential velocity $u_t(y)$ is observed on the surface of the plate. In order to enforce the no-slip boundary condition in the context of the present algorithm we need to eliminate this tangential velocity induced by the vortices in the wake, while maintaining the no-through-flow condition. By taking the limit of (21*a*) a vortex sheet of strength γ is observed on each side of the plate as

$$\left.\begin{aligned} \gamma(x = 0^-, y) &= -\tfrac{1}{2}\kappa(y) + u_t(y), \\ \gamma(x = 0^+, y) &= +\tfrac{1}{2}\kappa(y) + u_t(y). \end{aligned}\right\} \tag{29}$$

The vortex sheet (γ) is composed of the spurious tangential velocity that needs to be nullified and of the singularity distribution (κ) used to enforce the no-through-flow boundary condition. This process is depicted schematically in figure 3. In order to effect its dual purpose the vorticity associated with the sheet is introduced *diffusively* into the flow. As discussed in further detail in KLP, this process would modify the circulation of the flow and hence it can be related to a vorticity flux as

$$\int_{t-\delta t}^{t} \int_{-L/2}^{L/2} \nu \frac{\partial \omega}{\partial x}\, \mathrm{d}y\, \mathrm{d}t' = -\int_{-L/2}^{L/2} \gamma(y)\, \mathrm{d}y. \tag{30}$$

This relationship helps us link the kinematic and the dynamic description of the flow in the present algorithm. We consider the vorticity flux to remain constant over each

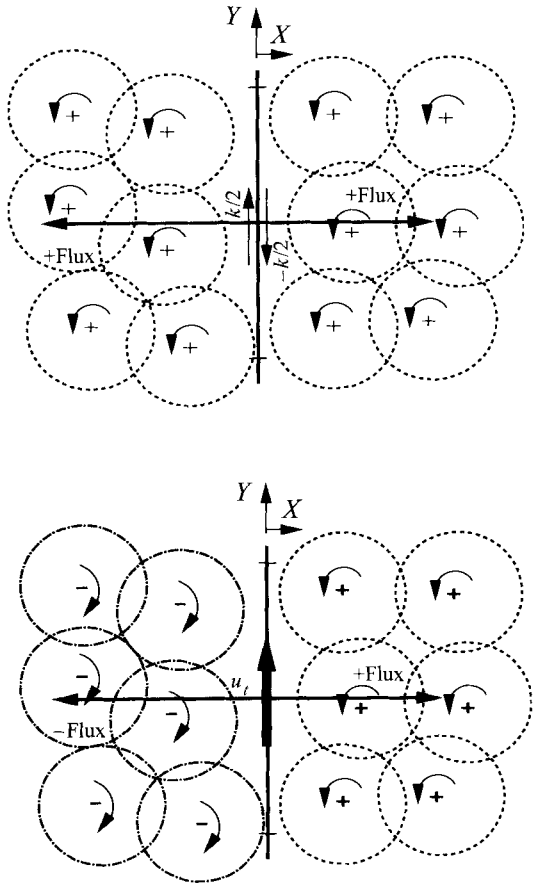

FIGURE 3. Sketch showing the distribution of the vorticity flux to the vortices in the domain to enforce the no-through flow (top) and no-slip (bottom) boundary conditions over each panel of the plate.

time step and we require that

$$\nu \frac{\partial \omega(y)}{\partial x} = -\frac{\gamma(y)}{\delta t}. \tag{31}$$

The vorticity flux helps establish a vorticity field on each side of the plate that eliminates the spurious tangential velocity u_t while simultaneously enforcing the no-through flow boundary condition via (29) and (31). This is achieved by solving the Neumann problem for the diffusion equation using an integral formulation (KLP).

The solution may be expressed as

$$\omega(\boldsymbol{x}, t) = \int_0^t \int_{-L/2}^{L/2} G(\boldsymbol{x}, t; \boldsymbol{\xi}, \tau)\, \mu(\boldsymbol{\xi}, \tau)\, \mathrm{d}s_\xi\, \mathrm{d}\tau \tag{32}$$

where $\mu(\boldsymbol{x}, t)$ is determined by the solution of

$$-\tfrac{1}{2}\mu(\boldsymbol{x}_s, t) + \int_0^t \int_{-L/2}^{L/2} \frac{\partial G}{\partial n}(\boldsymbol{x}_s, t; \boldsymbol{\xi}, \tau)\, \mu(\boldsymbol{\xi}, \tau)\, \mathrm{d}s_\xi\, \mathrm{d}\tau = \nu \frac{\partial \omega}{\partial n}(\boldsymbol{x}_s, t) \tag{33}$$

with

$$G(x,t;\xi,\tau) = \frac{1}{4\pi\nu(t-\tau)} \exp\left(-\frac{|x-\xi|^2}{4\nu(t-\tau)}\right). \tag{34}$$

We use an asymptotic expansion for small δt to calculate the integral in (33) explicitly. The surface of the plate is divided into M equidistant panels of size d, centred at y_m. Over each panel we assume a piecewise-constant distribution of the vortex sheet and the associated vorticity flux. The integral operator in (32) is discretized using as quadrature points the locations of the particles so that their strength is updated according to the following algorithm:

$$\Gamma_i^{n+1} = \Gamma_i^{n+1/2} + \frac{h^2}{2} \sum_{m=1}^{M} \gamma(y_m) \Phi(x_i - y_m \hat{e_y}, \delta t) \tag{35}$$

where

$$\Phi(x(x,y), \delta t) = \frac{e^{-x^2/4\nu\delta t}}{(4\pi\nu\delta t)^{1/2}} \left[\operatorname{erf}\left(\frac{d+y}{(4\nu\delta t)^{1/2}}\right) + \operatorname{erf}\left(\frac{d-y}{(4\nu\delta t)^{1/2}}\right)\right].$$

For further details the reader is referred to KLP. The influence of the vortex sheet decays with the distance from the plate so only the particles in the neighbourhood of the plate are affected, hence the computational cost of this step scales as $M \log N$.

4.2. *On the simultaneous enforcement of the no-through-flow and no-slip conditions*

The vortex sheet strength distribution (γ) in (29) is such that the introduction of vorticity in the flow field via the associated vorticity flux (31), (35) does not violate the no-through-flow condition. Owing to this fortuitous result, no through flow is enforced at the end of both sub-steps of the fractional step algorithm presented in this Section. We have exploited this result in order to reduce the computational cost of our method, while maintaining its accuracy. This is facilitated by the use of an Adams–Bashforth scheme for the advancement of the particle locations.

During the course of the simulation we explicitly enforce the no-through-flow condition only at the end of the second sub-step, along with the no-slip condition. One may observe then that at the beginning of the following convection sub-step (during the calculation of the Biot-Savart integral) the velocity induced by the vortices on each other is always computed in a no-through-flow configuration. Hence the motion of the vortices can be computed, using an Adams–Bashforth integration formula, without explicitely accounting for the surface singularity. However as soon as the vortices are displaced a slip and through velocity appear on the surface of the plate. At the end of the second sub-step however the two components of the spurious velocity are eliminated, as discussed above, and this procedure is repeated during the course of the simulation.

We have conducted simulations that enforce the no-through-flow at both sub-steps by explicitly accounting for the vortex sheet singularity (23) to enforce the no-through-flow condition. Their results are indistinguishable from the results obtained using the strategy described in the previous paragraph. As the second option reduces the computational cost it has been employed in the majority of our simulations and particles were not observed to cross the surface of the plate. An equivalent result, regarding the simultaneous enforcement of the no-slip and no-through-flow boundary conditions in the context of this algorithm, is valid for the case of the flow past bodies of non-zero thickness (Pépin 1990).

Note that when an integration scheme requiring multiple steps (such as Runge–Kutta) is used to integrate (24), the explicit use of the surface singularity (κ) is necessary to enforce no through flow after the first step of the integration. Also as (24) refers to the Lagrangian locations of the particles, a Runge–Kutta scheme of order 2 is used to integrate the particle locations after remeshing, using the procedure described in §4.1.

4.3. *Initialization*

Initially the particles are placed in the centre of the cells of a rectangular equi-spaced grid, surrounding the flat plate. At time $t = 0^-$ the strength of these particles is set to zero. At the onset of motion ($t = 0^+$), a through flow is observed on the surface of the plate – constant along its surface and equal to $\boldsymbol{U}_b(0^+)$. In order to counteract this through flow we introduce a vortex sheet on the surface of the plate whose strength is (22*a*)

$$\kappa(\theta) = -2\,\boldsymbol{U}_b(0^+)\,\frac{\cos(\theta)}{\sin(\theta)}. \tag{36}$$

As initially the particles have zero strength (null vorticity field) there is no contribution from the Biot-Savart integral. According to the fractional step scheme described in §4.1, we may compute a velocity field at the location of the particles based on the strength of the vortex sheet. Note however that this would have no effect on the vorticity field as during this step the strength of the vortices remains constant and equal to zero. The tangential velocity (u_t) induced on the surface of the plate from the vortices in the wake is zero as well so (29) for the vortex sheet (γ) reduces to

$$\gamma(x = 0^-, y) = -\tfrac{1}{2}\kappa(y), \quad \gamma(x = 0^+, y) = +\tfrac{1}{2}\kappa(y). \tag{37}$$

In the following sub-step the vortex sheet is diffused into the flow field, as described in the second part of our algorithm (35). The vortices surrounding the plate attain a strength such that they induce a normal velocity u_n to counteract the spurious through velocity, while the no-slip boundary condition is trivially satisfied (see also figure 3). After the vortices have acquired a non-zero strength the simulation proceeds as discussed in the previous subsection.

5. Results

In this section we present the results of our simulations for the early stages of the evolution of the flow behind an impulsively started and uniformly accelerated flat plate. We conduct a convergence study of our numerical method and we compare our results with related theoretical and experimental works, using diagnostics such as the streamlines, the vorticity field, the length of the recirculating wake and the drag coefficient of the flow. For the case of the uniformly accelerated plate our results confirm an instability that has been observed in related experimental studies and we present a series of calculations and diagnostics to quantify our observations. The results reveal a similarity law for the uniformly accelerated flows.

5.1. *The impulsively started flat plate*

The first part of our work concerns simulations for an impulsively started flat plate over a range of Reynolds numbers. The Reynolds number (Re) of the flow is defined based on the length of the plate (L) (figure 1), as

$$Re = \frac{UL}{\nu} \tag{38}$$

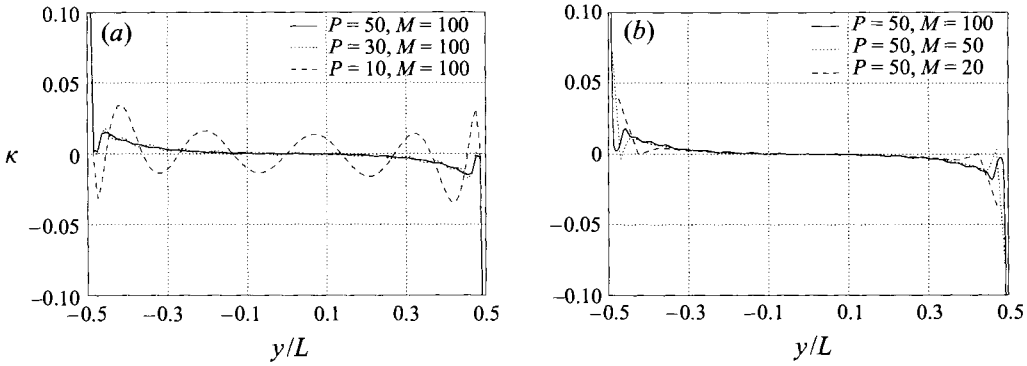

FIGURE 4. Convergence study of the influence of (*a*) the number of terms (P) in the Fourier series expansion and (*b*) M (number of panels), on the computation of κ.

and the time (t) is non-dimensionalized for the impulsively started case as

$$T = \frac{Ut}{L}. \tag{39}$$

The drag coefficient (c_D) of the body is given then by

$$c_D = -\frac{2\boldsymbol{F}_b \cdot \hat{\boldsymbol{e}}_x}{U_\infty^2 L} \tag{40}$$

where $\boldsymbol{F}_b$ is calculated by

$$\boldsymbol{F}_b = \frac{\mathrm{d}}{\mathrm{d}t}\int_{\mathrm{flud}} \boldsymbol{\omega} \times \boldsymbol{x}\,\mathrm{d}\boldsymbol{x} = \frac{\mathrm{d}}{\mathrm{d}t}\sum_{i=1}^{N} \Gamma_i\, \boldsymbol{x}_i \times \hat{\boldsymbol{e}}_z \tag{41}$$

where $\boldsymbol{x}_i = (x_i, y_i)$ is the location and Γ_i the strength of the vortices in the wake (Koumoutsakos & Leonard 1995).

The main features of an impulsively started flow are common for all the Re that are presented in this work. Two counter-rotating vortices appear in the wake. They are fed by a shear layer emanating from the tips of the plate and induce a secondary vorticity region in the rear of the plate at the early stages of the flow. At later times the feeding shear layers are spread by the action of diffusion and eventually become part of the vortex while the secondary vorticity region is weakened. Note the absence of any secondary separation to the rear of the plate in the present simulations.

Vorticity contours of $(0, \pm 0.5, \pm 1.0, \pm 1.5, \pm 2.0, \pm 4.0, \cdots)$ and streamlines of $(0, \pm 0.2, \pm 0.4, \cdots)$ are presented. We discuss the evolution of the flow and we compare with several experimental works and related numerical solutions of the steady state of the flow.

5.1.1. *Convergence study*

The accuracy of the numerical solution was examined by varying the parameters of our computational scheme, such as the blob size, the time step, the number of panels, the number of terms kept in the Fourier series expansion for κ and the remeshing frequency. The first two parameters in this list were linked as optimum results were obtained for the approximation of the diffusion operator when using a core radius such that

$$\epsilon = (2\delta t/Re)^{1/2}. \tag{42}$$

A particle overlap ratio of $h/\epsilon \approx 0.8$ was maintained. To monitor the convergence we used the streamlines, velocity profiles, the vorticity field and the drag coefficient of the plate.

First we examined the effect of the number of terms (P) kept in the expansion (22*a*) for κ and the effect of the number of panels (M) used in the enforcement of the no-through-flow boundary condition. We considered the impulsively started flow at $Re = 126$, and we conducted a high-resolution simulation until $T = 8.0$. In order to further continue the calculation we need to perform the two sub-steps discussed in §4. The effects of P and M on the accuracy of the calculation is demonstrated by considering the solution of (22*a*) during the first sub-step of our algorithm. A particular normal velocity profile ($u_n(y)$) is established after the particles are convected due to their mutual interaction and the task is to determine a vortex sheet κ so as to nullify this through flow on the surface of the plate. In figure 4(*a*) we keep constant the number of panels used to compute the right-hand side of (22*a*) and we observe the convergence of the solution of the equation as we vary the number of terms in the expansions. In figure 4(*b*) we maintain a relatively high number of terms in the expansions and we vary M. Note that the convergence is slower at locations near the tips of the plate due to the singularity of the velocity field. In order to examine the effect of the temporal and spatial discretization of our scheme, the computations were run with time steps (δt) of 0.005,0.02,0.032 and 0.05. Both spatial and temporal refinement are tested with these cases due to the link between the time step and core radius ϵ (42). In figure 5(*a*) we present the vorticity field (top part) and the streamlines of the flow at $T = 8$. As expected the streamlines exhibit a faster convergence rate, suggesting that the vorticity field is a more reliable diagnostic for the accuracy of the numerical scheme. Of particular interest is the behaviour of the recirculating bubble. One may observe that the bubble length and centre of the recirculating vortex are relatively insensitive to the refinement of the calculation (see also figure 5*b*) despite the discrepancy in the details of the vorticity contours as the resolution increases. In figure 5(*c*) we present the magnitude of the velocity field along the centreline of the plate. One may observe the faster convergence rate of the velocity field, in the upstream (practically inviscid) part of the domain. In figure 5(*d*) we show the results of our convergence study on the drag coefficient. Note that an order of magnitude decrease of the resolution of the flow results only in a 5% loss of accuracy in the calculation of the drag coefficient.

As a further verification test of our scheme, a flat plate aligned with the flow at $Re = 500$ was simulated to $T = 5.0$ for comparison of the drag coefficient with triple-deck analysis. Figure 6 reveals convergence of our unsteady solution to the steady triple-deck prediction (Messiter 1970; Stewartson 1974) given by

$$c_f = \frac{1.328}{Re^{1/2}} + \frac{2.668}{Re^{0.875}}. \tag{43}$$

The parameters for this simulation were: $\delta t = 0.005$, $P = 50$, $M = 220$, with other values as specified above.

Finally in order to test the effect of the remeshing frequency we conducted a series of simulations for the early stages of the development of the flow at $Re = 126$. We maintained a time step of $\delta t = 0.005$ and we remeshed every 6, 12 and 24 steps. The effect of remeshing on the drag coefficient is shown in figure 7. Note that remeshing even every 24 time steps produced relatively accurate results. The high-frequency oscillations observed on the drag coefficient are attributed to the effect of remeshing on the linear impulse of the flow. That is, the remeshing scheme conserves the linear

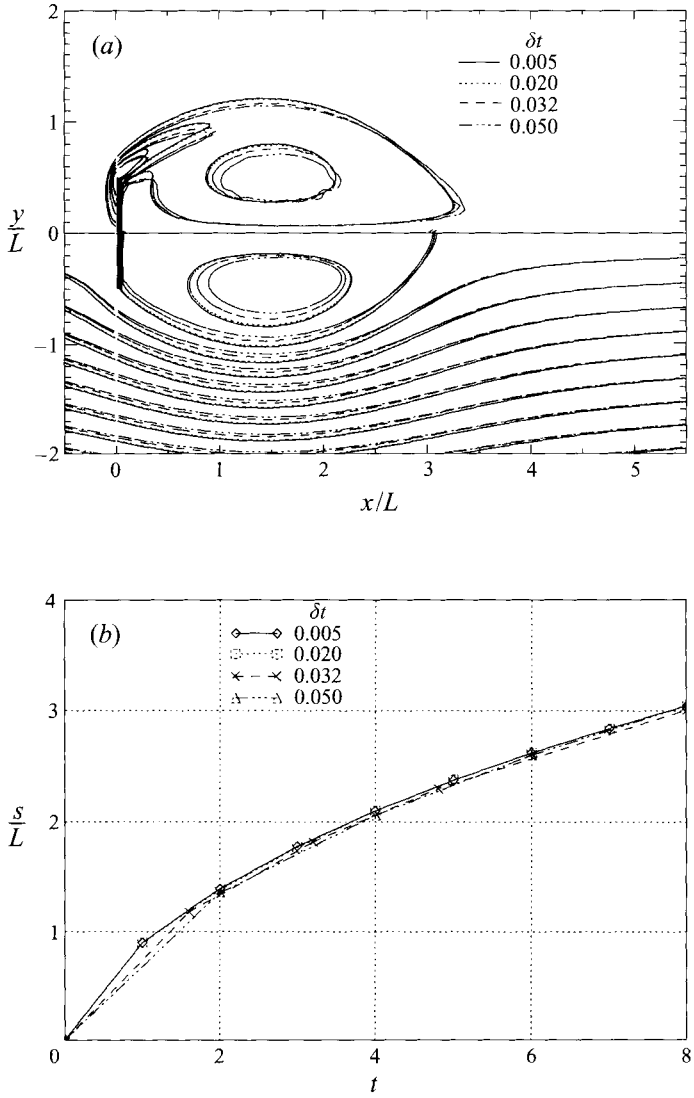

FIGURE 5(*a,b*). For caption see facing page.

impulse, but not its time derivative (i.e. the drag coefficient). It appears, however, that this effect does not affect the global characteristics of the flow. During our calculations remeshing was performed as dictated by conservation of the global quantities of the flow field, such as circulation and the y-component of the linear impulse but we always maintained a maximum remeshing frequency of 10 steps.

The parameters of the computations for the simulations presented herein were chosen based on the convergence study conducted above and are summarized in table 1.

The present results concern the unsteady, symmetric early time development of the flow. Note however, that no symmetry constraint was imposed in our computations. In fact the preservation of flow symmetry serves as evidence for the accuracy of the results of our simulations.

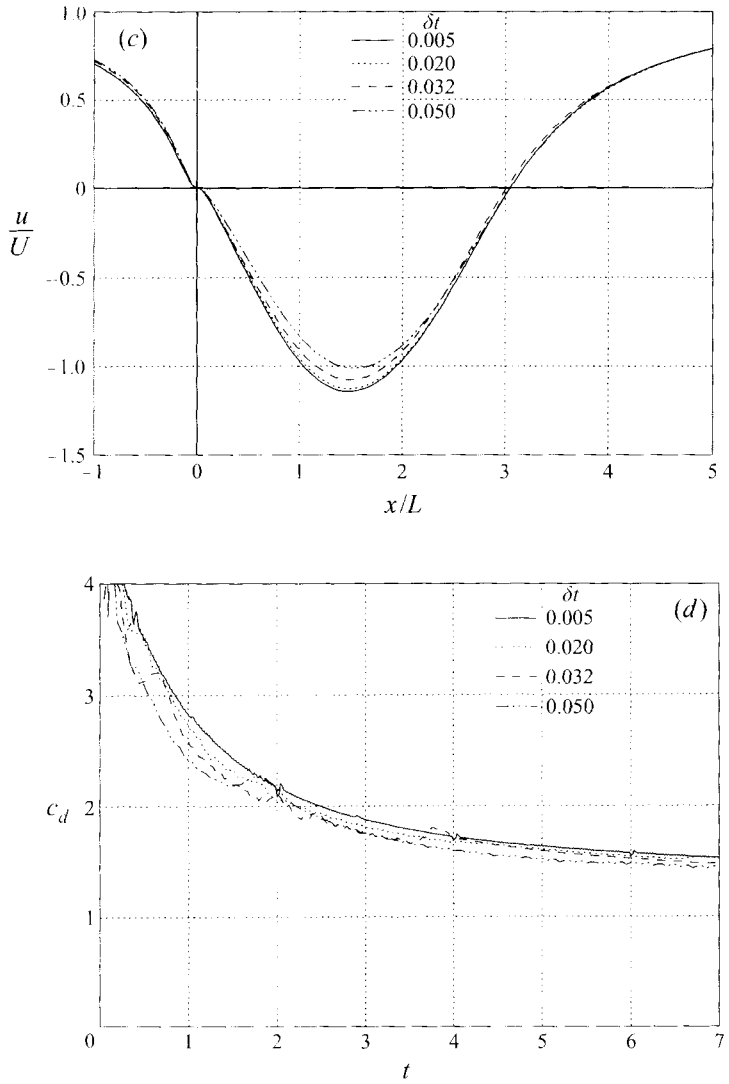

FIGURE 5. Effect of the variable resolution on (*a*) the streamlines (bottom part) and vorticity contours (upper part) of the flow at $T = 8$, (*b*) the evolution of the recirculating bubble length, (*c*) the velocity profile along the axis of symmetry ($y = 0$) of the plate, (*d*) the evolution of the drag coefficient.

5.1.2. $Re = 20$

The development of the vorticity field and the streamlines presented in figure 8. One may observe that at earlier times ($T \leqslant 2$) the flow develops rapidly with the primary vortices emanating from the tips of the plate introducing a secondary vorticity in the rear of the plate. However beyond a certain time ($T \approx 6$) the flow remains almost unchanged as a stable configuration is assumed by the primary and the secondary vorticity and the length of the recirculating bubble remains unchanged beyond this time.

An extensive experimental study of this flow at $Re = 20$ has been carried out by CL (Dennis *et al.* 1993). In figure 9 we overlay the streamlines of the computations on the

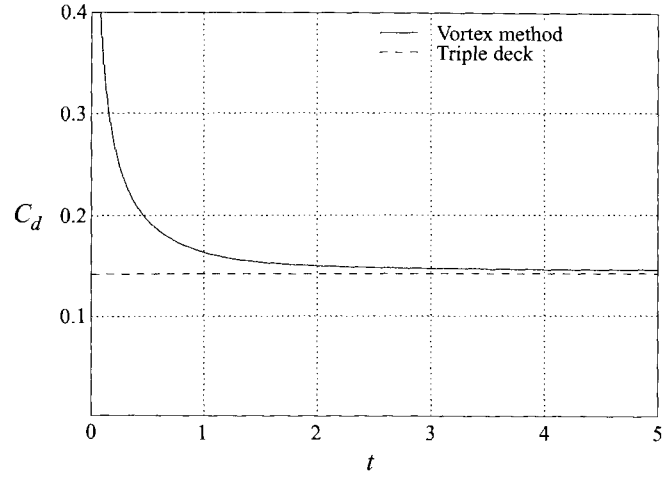

FIGURE 6. Comparison of the asymptotic behaviour of the drag coefficient to the triple-deck prediction for $Re = 500$ steady flow over a plate aligned with the flow.

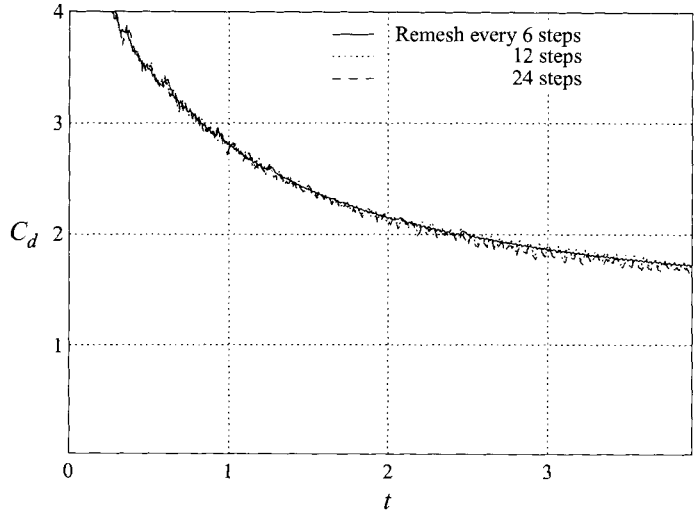

FIGURE 7. Effect of remeshing on the evolution of the drag coefficient.

Re	δt	P	M
20	2×10^{-2}	30	50
40	1×10^{-2}	40	60
126	5×10^{-3}	75	100
1000	1×10^{-3}	100	650

TABLE 1.

streaklines reported by Dennis *et al.* with $b = 0.15$. A discrepancy appears especially at the later times of the evolution of the flow. Note that a finite blockage ratio and the possible influence of three-dimensional effects distinguishes the experimental results from the present calculations. In figure 10 we present a comparison of the

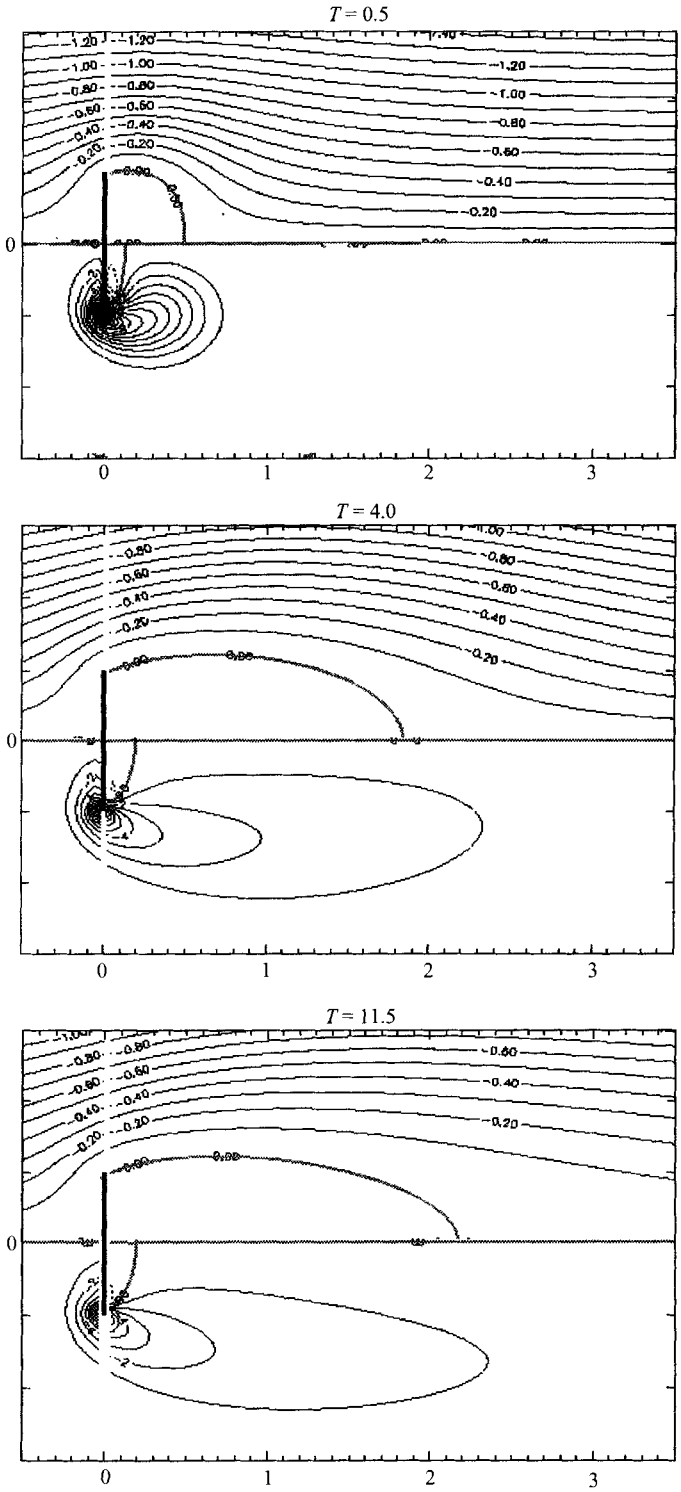

FIGURE 8. Vorticity (lower part) and instantaneous streamline (upper part) contours for an impulsively started flat plate at $Re = 20$.

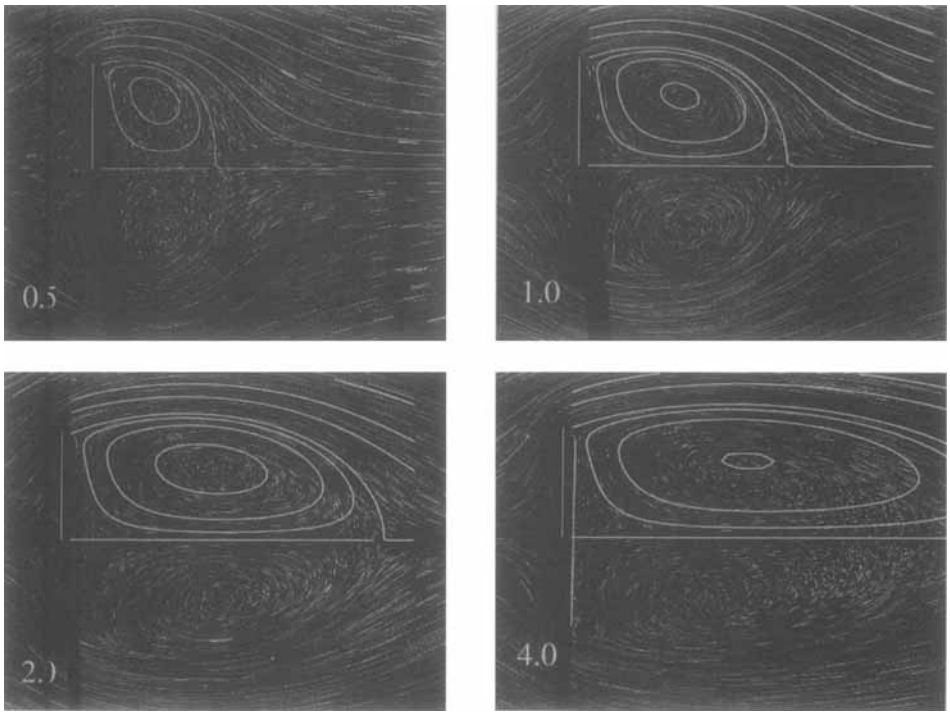

FIGURE 9. Comparison of instantaneous streamlines (computations) ($b = 0$) and streaklines (Dennis *et al.* 1993) ($b = 0.15$) for an impulsively started plate at $Re = 20$.

velocity profiles at the rear axis of the plate as calculated by the experiments and the computations. Note that for the early time ($T = 0.5$) when the channel walls do not significantly affect the flow good agreement is observed between the experimental and the computational results, especially outside the recirculating region. The finite blockage ratio is manifested in that the experimental value of the maximum velocity is consistently larger than the respective computational results (corresponding to an infinite domain). The agreement deteriorates with time with the experimental values consistently predicting a smaller value for the length of the recirculating region. Note that a similar behaviour has been observed by Coutanceau & Bouard (1977) for the case of a circular cylinder. In figure 11 we present the time evolution of the length of the recirculating region. The results of Dennis *et al.* for two different blockage ratios ($b = 0.1$ and $b = 0.15$) suggest that the recirculating bubble would be larger for an infinite domain than for a plate in a channel and seem to validate the results of the present computations. We present also the experimental results of Taneda & Honji (1971) for similar Re ($Re = 18.1$ and 24.3). Note that for early times all experimental and computational results are in good agreement. However Taneda & Honji's results for $Re = 24.3$ seem to overpredict the recirculating bubble as compared with the other works. As suggested by Taneda & Honji (1971), this discrepancy may be attributed to the three-dimensionality that is observed in their experiments. Their results at $Re = 18.1$ seem to be in good agreement with the present computations although they are not extended to the steady state regime.

In figure 12 we present the vorticity field as computed by the present method at $T = 11.5$ and as computed by the steady-state calculations of Dennis *et al.* (1993). The discrepancy in the results suggest that the vorticity field relaxes much

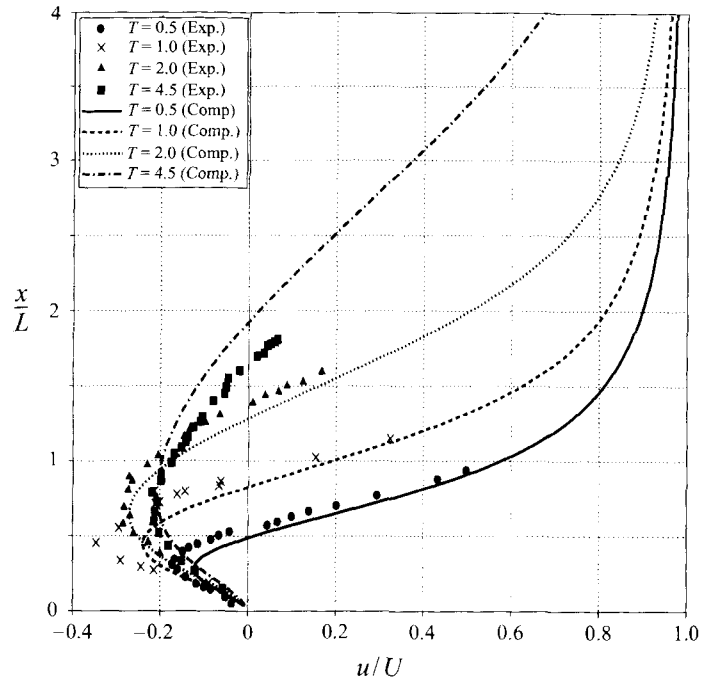

FIGURE 10. Evolution of the velocity profile at the rear of the flat plate at $Re = 20$.

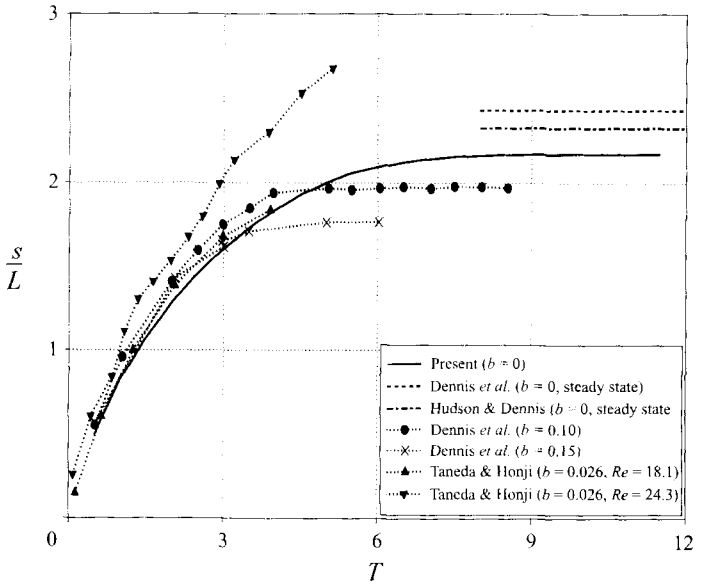

FIGURE 11. Evolution of the wake bubble behind an impulsively started flat plate at $Re = 20$. Comparison of experimental and computational results.

slower to the steady state than diagnostics such as the bubble length and the drag coefficient. However discrepancies of similar magnitude have been observed with other diagnostics presented by Dennis *et al.* (1993). For example in figure 11 we show the steady-state length of the recirculating bubble as computed by Hudson & Dennis (1985), Dennis *et al.* (1993). A 10% to 20% discrepancy appears between the

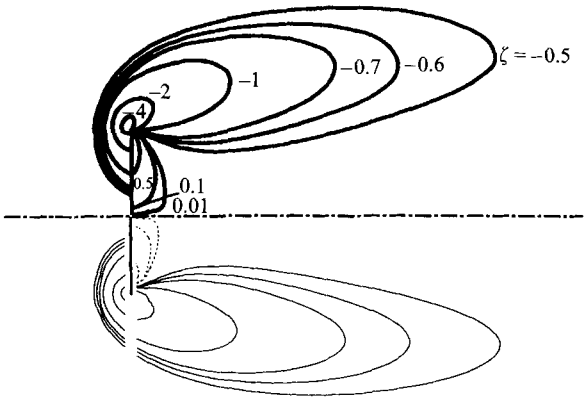

FIGURE 12. Vorticity field of an impulsively started plate at $Re = 20$. Top part: Steady state (Dennis *et al.* 1993), Bottom part : $T = 11.5$ (present results).

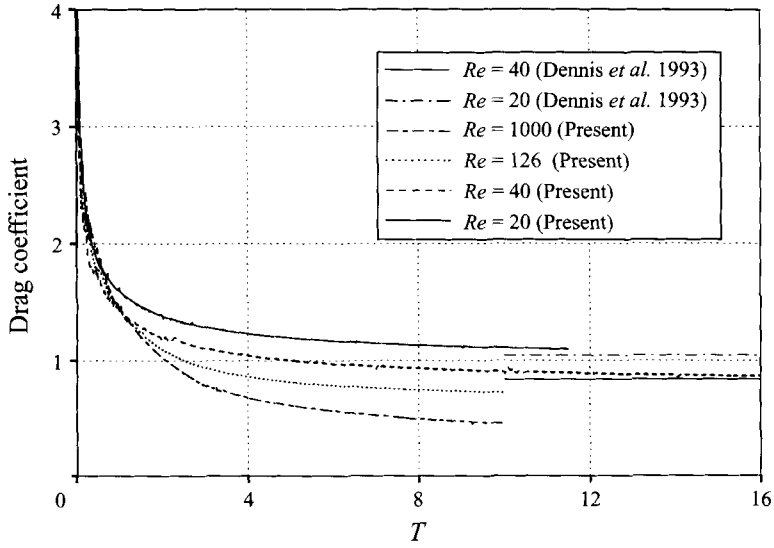

FIGURE 13. Evolution of the drag coefficient behind an impulsively started flat plate, for $Re = 20$, 40, 126, 1000. Comparison with steady-state results (Dennis *et al.* 1993).

steady-state computations and the asymptotic state of the present calculations. ITM have carried out experiments with $b = 0.067$ that are in excellent agreement with their steady-state calculations as well as with the asymptotic behaviour of the present simulations. The observed discrepancies among the various steady-state calculations may be attributed mainly to the different treatment of the far-field condition. Far-field boundary conditions may be viewed as introducing a 'numerical channel' in the simulation of the flow around the flat plate. Note however that ITM use a far-field condition that has been devised by Fornberg (1980) and has been shown to render accurate results for a variety of flows (Fornberg 1980; Natarajan, Fornberg & Acrivos 1993). In the present scheme the far field condition is not interfering with the physics of the problem as it is explicitly enforced by the use of the Biot-Savart law to compute the velocity field.

In figure 13 the drag coefficient as computed by the present scheme is observed to

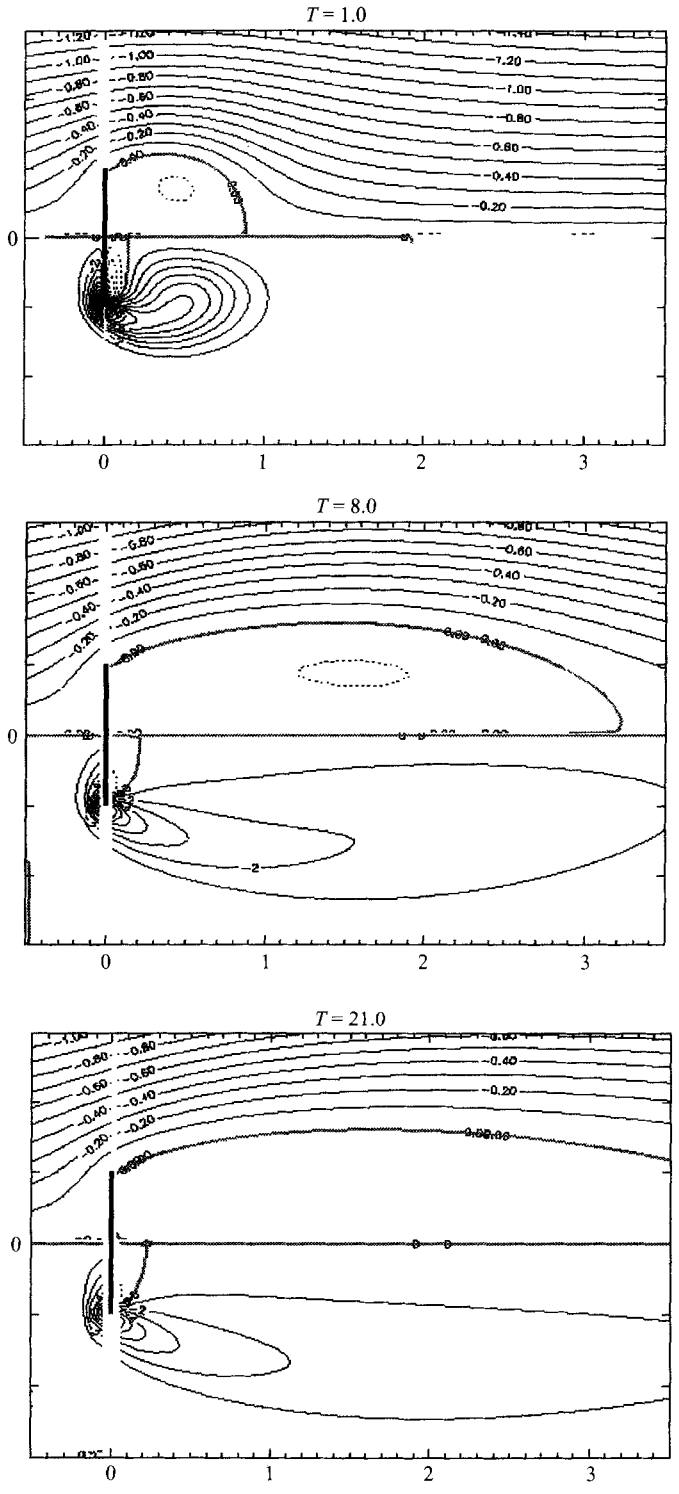

FIGURE 14. Vorticity (lower part) and streamline (upper part) contours for an impulsively started flat plate at $Re = 40$.

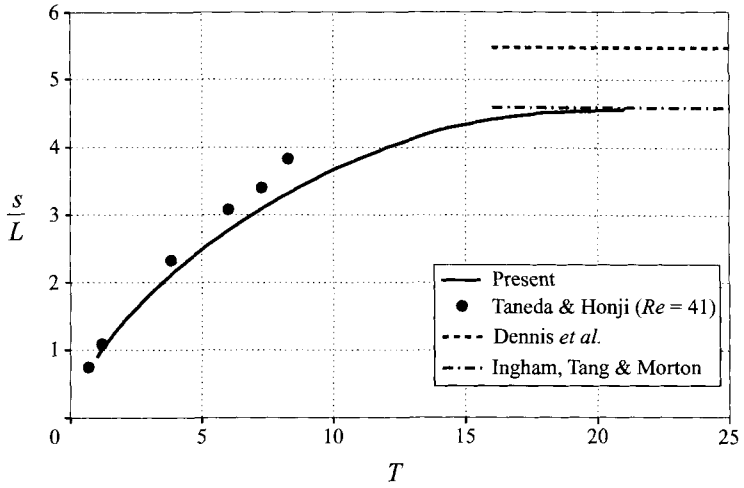

FIGURE 15. Evolution of the wake bubble behind an impulsively started flat plate at $Re = 40$.

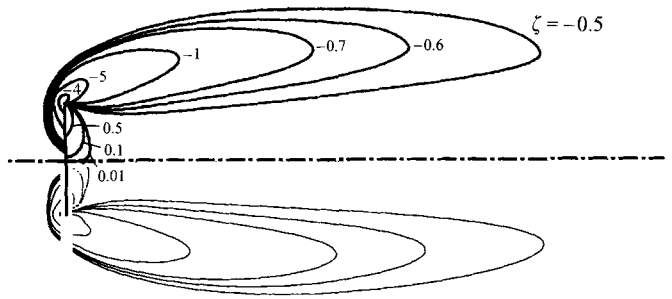

FIGURE 16. Vorticity field of an impulsively started plate at $Re = 40$. Top part: Steady state (Dennis *et al.*), Bottom part : $T = 21.0$ (present results)

approach the value of the steady-state results as computed by Dennis *et al.* (1993). The drag coefficient was computed by Dennis *et al.* by considering the momentum balance of the fluid between the plate and any surrounding contour. They observed that the drag coefficient is constant, provided that the surrounding contour is not approaching the end of the computational domain. The results of the present computations for the drag coefficient are in a far better agreement with the steady-state predictions than the results for the length of the recirculating bubble. This is attributed to the fact that unlike the length of the bubble the drag coefficient is a global quantity of the flow and hence not so sensitive to the details of the flow field.

5.1.3. *Re = 40*

The evolution of the vorticity field and the streamlines for $Re = 40$ is presented in figure 14. As the Re increases stronger vortices are formed at the tips of the plate thus inducing a stronger secondary vorticity the rear of the plate. This secondary vorticity is trapped in the recirculating region of the flow and is eventually eliminated by the effects of viscosity as the centres of the pimary vortices move away from the centre of the plate. The evolution of the length of the bubble is presented in figure 15 and is compared with the experimental results of Taneda & Honji (1971) for $Re = 41$, and the steady-state results of Dennis *et al.* (1993). Excellent agreement of the computational and experimental results is obtained for the early times.

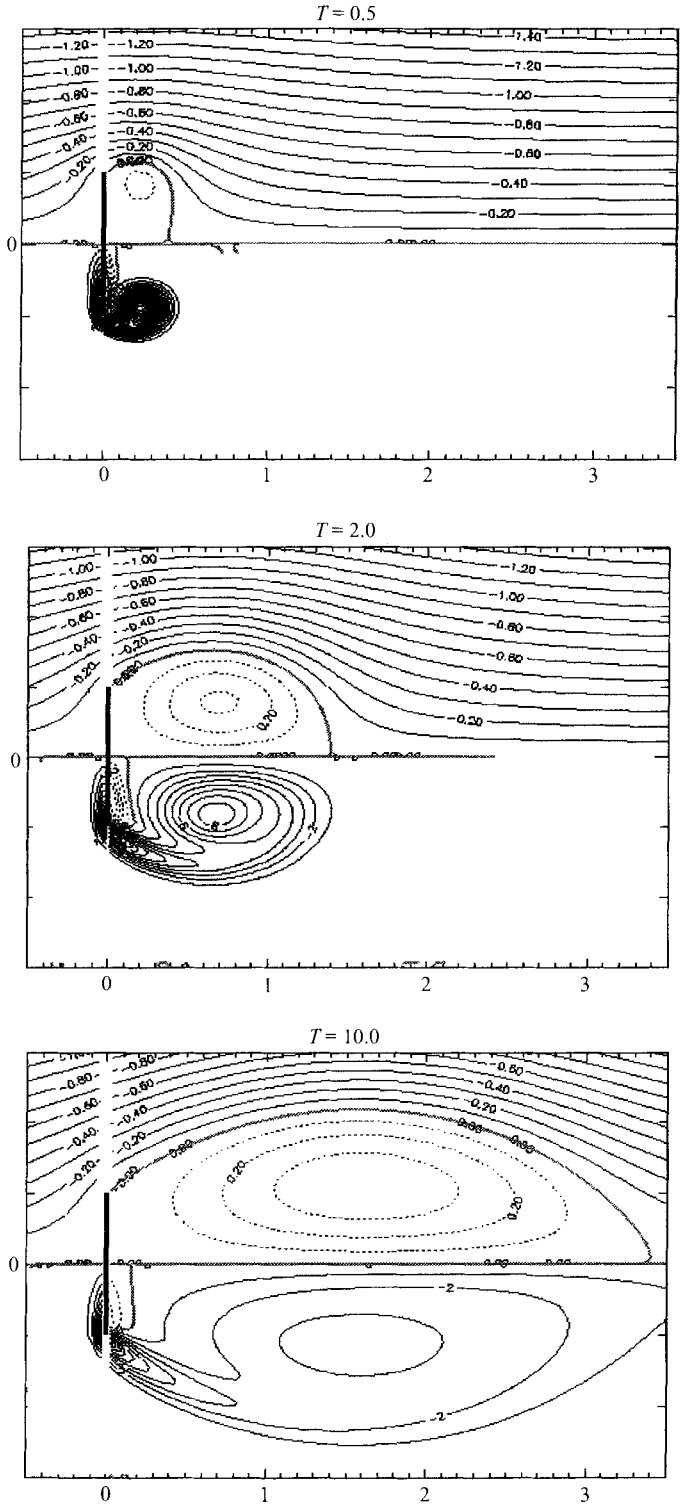

FIGURE 17. Vorticity (lower part) and streamline (upper part) contours for an impulsively started flat plate at $Re = 126$.

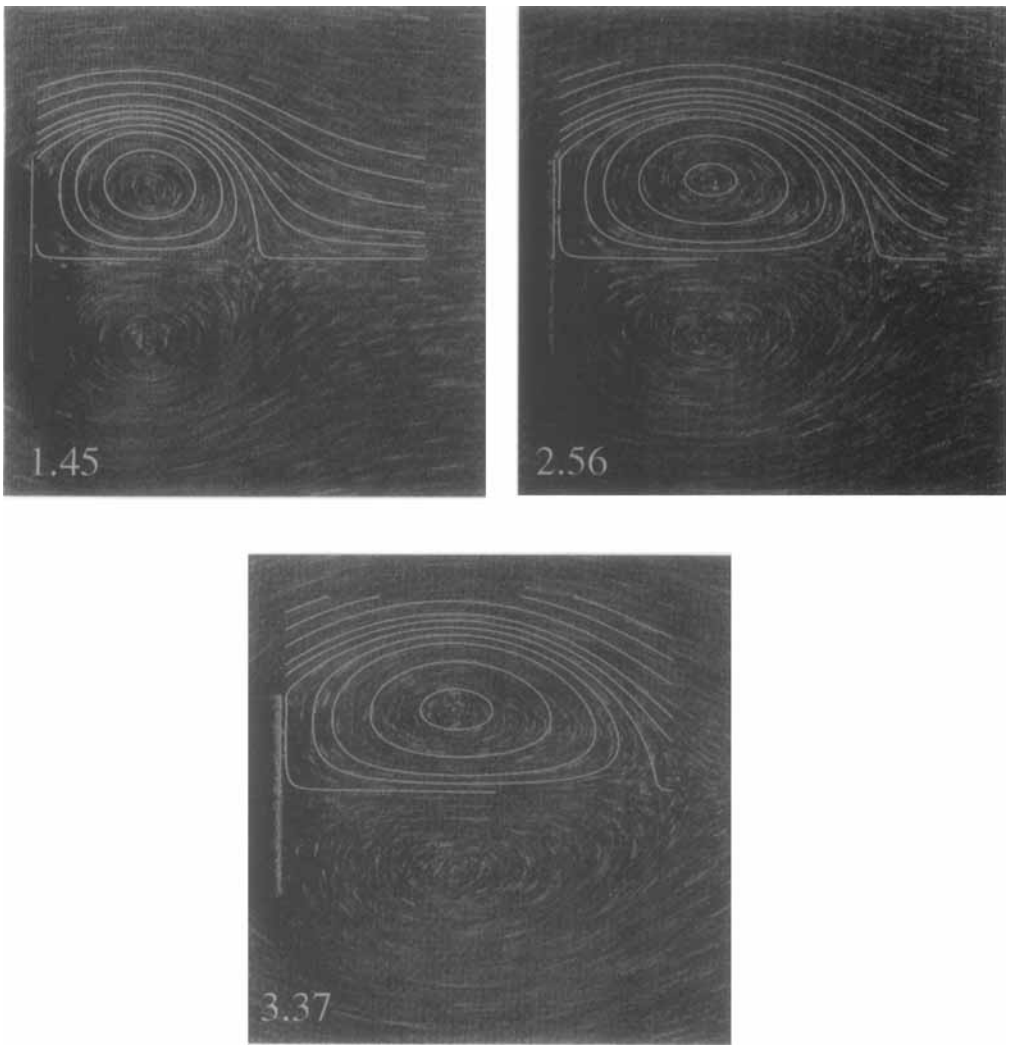

FIGURE 18. Comparison of instantaneous streamlines (computations) ($Re = 126$, $b = 0$) and streaklines (Taneda & Honji 1971) ($Re = 125.4$, $b = 0.026$) for an impulsively started plate at $T = 4.0$.

Taneda & Honji (1971) have observed that their flow would become asymmetrical at about $T = 10$. The steady-state results of Dennis *et al.* predict a recirculating bubble which is about 20% larger than the value predicted (experimentally and numerically) by ITM and the results for the asymptotic state of the wake of the present calculations. The theoretical and experimental steady-state results of ITM are in excellent agreement with the predictions of the present simulations. Note that the present formulation and the one employed by ITM differ significantly. Ours is an unsteady computation with an explicit handling of the far-field boundary condition whereas ITM conduct steady-state simulations, employing analytic forms for the enforcement of the far-field boundary conditions. We believe that this independent reproduction of our results provides a strong validation of our technique. Moreover it suggests that the far-field approximations used by ITM (formulated by Fornberg

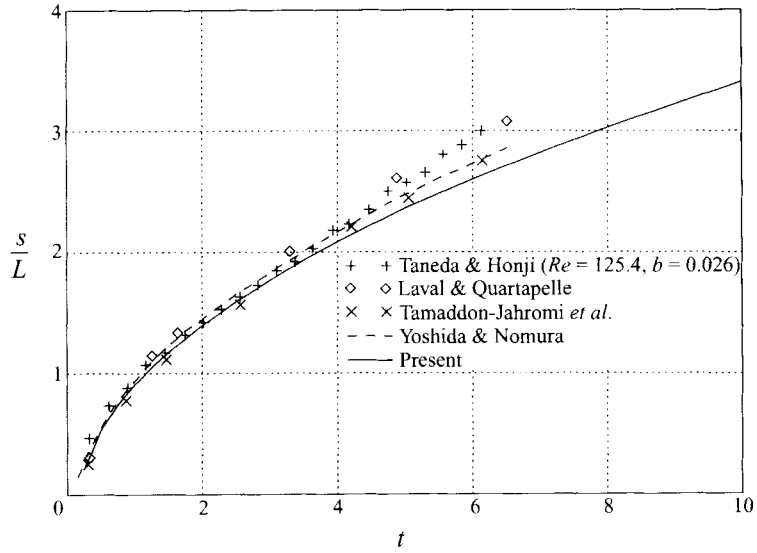

FIGURE 19. Evolution of the wake bubble behind an impulsively started flat plate at $Re = 126$. Comparison of experimental and computational results.

1980) may be used for accurate steady-state calculations of other types of bluff body flows.

One also may observe the excellent agreement of the vorticity contours as computed by the present scheme (at $T = 21$) and the steady-state results of Dennis *et al.* (figure 16). The drag coefficient asymptotes to a value which is in excellent agreement with the results of their steady-state calculations (figure 13). As was noted above however, the drag coefficient is a global quantity for the steady-state calculations whereas the length of the recirculating bubble is a local quantity of the flow.

5.1.4. *Re = 126*

In figure 17 we present the vorticity field and the streamlines of the unsteady flow at $Re = 126$. The topology of the flow does not differ significantly from that observed at lower Re numbers although the secondary vorticity is more active due to the stronger vortices being formed at the tips of the plate. The results of the present computations at $Re = 126$ for the streamlines are shown in figure 18 along with the streaklines of Taneda & Honji (1971) for $Re = 125.4$. Note that the present experimental and computational results are in closer agreement than the corresponding results shown in figure 9. This may be attributed to the smaller blockage ratio in the experiments of Taneda & Honji ($b = 0.026$) compared to that of Dennis *et al.* ($b = 0.15$).

In figure 19 we present the length of the recirculating bubble as computed by the present scheme and compare it with the experimental results of Taneda & Honji (1971) and the computational works of Tamaddon-Jahromi *et al.* (1994), Laval & Quartapelle (1990) and Yoshida & Nomura (1985). These computations are mostly concerned with the long-time behaviour of the flow, when shedding has been established.

The computational results are in good agreement with the experimental ones although deviations seem to appear at later times. It is suspected that this is a manifestation of three-dimensional effects and the onset of asymmetry in the experiments.

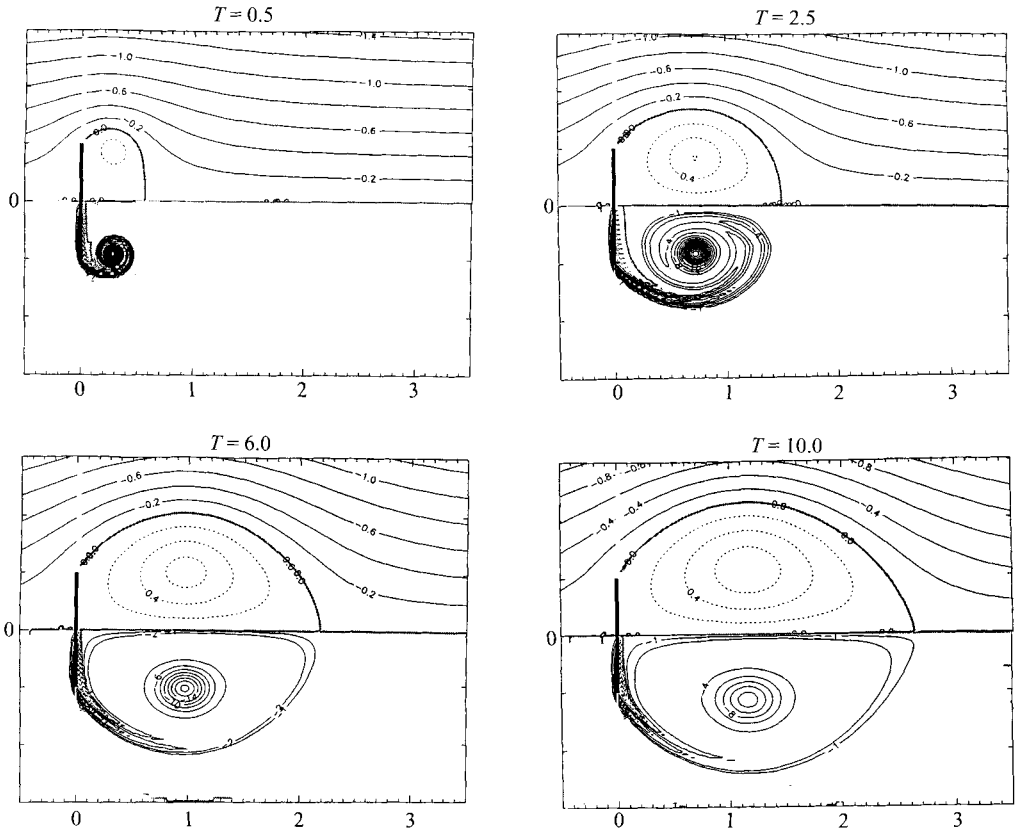

FIGURE 20. Vorticity (lower part) and streamline (upper part) contours for an impulsively started flat plate at $Re = 1000$.

5.1.5. *Re = 1000*

This is the highest *Re* for which computations were carried out in this study. The increase in the Reynolds number requires a larger number of computational elements to efficiently resolve the steeper gradients of the flow. This implies a respective decrease in the time step of the present simulations. A time step of 0.005 was used along with a panel size of 0.001 resulting in approximately half a million computational elements at the end of the simulations. In figure 20 we present the evolution of the vorticity field and the streamlines. Two distinct almost circular vortices are formed behind the plate inducing a strong secondary flow. The secondary vorticity is displaced further towards the outer edge of the flow while the feeding vortex layer of the vortices is thinned out. The initial primary vortices that were formed reside in the centre of the recirculating region behind the plate acting as if almost separated from the rest of the flow.

Note that unlike the lower *Re* cases, the secondary vorticity in the back of the plate remains stronger at later times and a thin layer is swept away from the back of the plate due to the influence of the primary vortex. This secondary vorticity layer is then separating along the primary shear layer. As the strength of the primary vortex is reduced by diffusion the strength of the secondary vorticity and its departure from the lee of the plate is diminished. This interplay of primary and secondary voticity might have implications for the inviscid modelling of flows with sharp separation points.

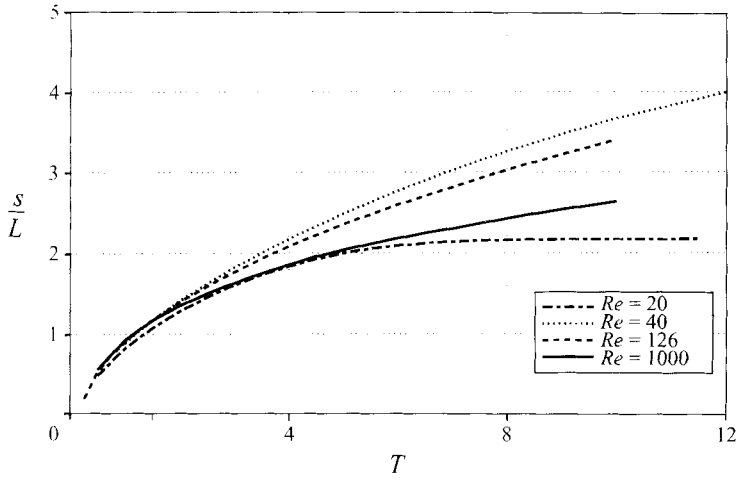

FIGURE 21. Evolution of the wake bubble behind an impulsively started flat plate, for $Re = 20, 40, 126, 1000$.

In figures 21 and 13 we present the evolution of the wake bubble and the drag coefficient for this and all other Re that we studied. It is interesting to observe that unsteady evolution of the drag coefficient exhibits a regular monotonic behaviour with respect to the Reynolds number (more obvious at later times). However such obvious behaviour is not evident in the evolution of the length of the wake. However the results for $Re = 1000$ and 126 are not steady-state results, so they describe transient behaviour of the wake bubble. One may infer that the drag coefficient assumes its steady-state value much faster than the respective length of the recirculating bubble.

5.2. *The uniformly accelerated flat plate*

In this section, we present results regarding a plate that is uniformly accelerated with an acceleration (a) normal to the direction of the flow. The dimensionless parameters of the flow are

$$T^* = \frac{a t^2}{L}, \quad \alpha = \frac{a L^3}{\nu^2}, \tag{44}$$

and the drag coefficient of the plate is non-dimensionalized as

$$c_D = \frac{2\boldsymbol{F}_b \cdot \hat{\boldsymbol{e}}_x}{(a t_f)^2 L} \tag{45}$$

where t_f is an arbitrary dimensional time. In order to compare the results of the various simulations we chose t_f so that $T_f^* = 25$ without any loss of generality. The viscosity for our computation was chosen to be $\nu = 0.025$, the time step was such that 200 time steps were taken to reach $T^* = 1.0$, the size of the vortex particles was chosen to be $\epsilon = (2\nu\delta t)^{1/2}$ and $M \approx 0.9L/\epsilon$ panels were used to discretize the body. We conduct a systematic study of the flow and compare our computational results with the experimental work of Taneda & Honji (1971). We discuss the underlying mechanisms of the flow and infer scaling laws for the drag coefficient and the length of the recirculating bubble. Vorticity contours of $(0, \pm 50, \pm 100, \pm 150, \pm 200, \pm 400, \pm 600, \cdots)$ are presented for $0 \leqslant T^* \leqslant 1$, and contours of $(0, \pm 50, \pm 150, \pm 300, \pm 600, \pm 900, \pm 1200, \cdots)$ are presented for later times.

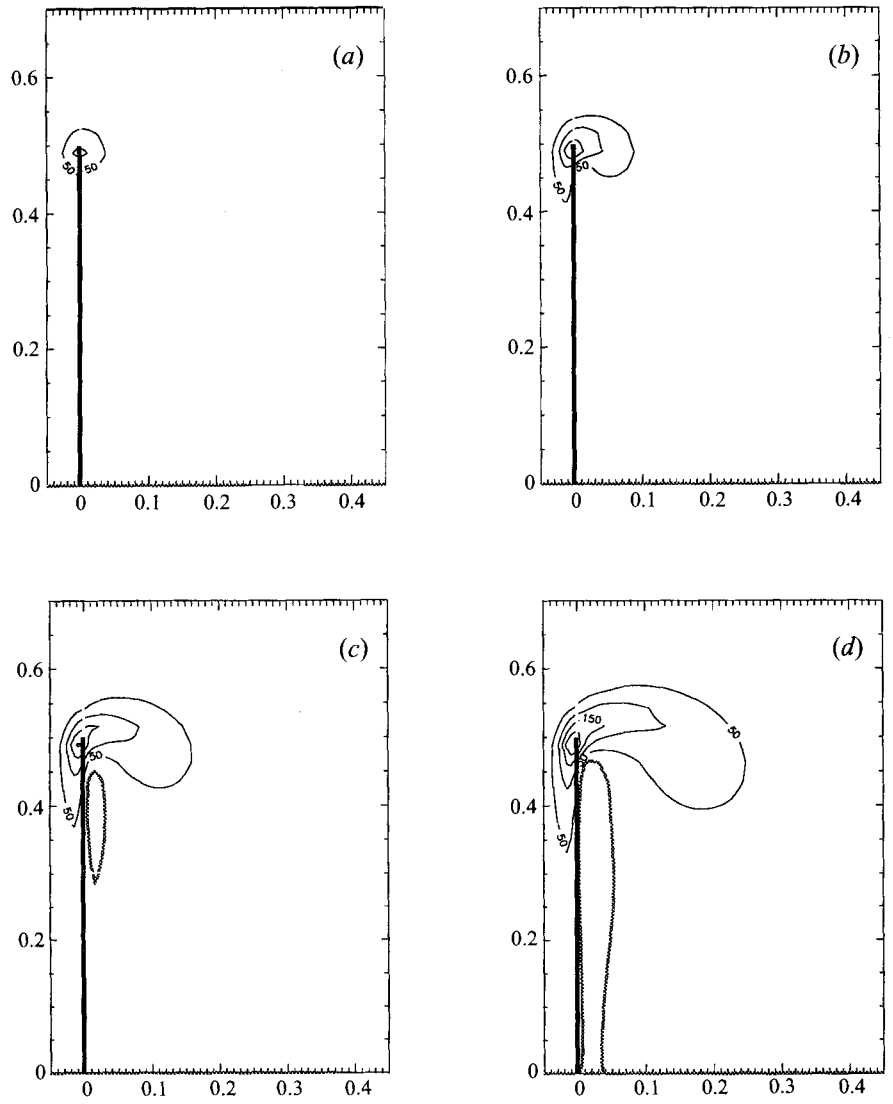

FIGURE 22. Early time evolution of the vorticity field for an accelerated flat plate ($a = 19.9375$). Vorticity field at $T^* = 0.04, 0.16, 0.36, 0.64$ (a–d)

5.2.1. $a = 19.9375\,(\alpha = 0.319 \times 10^5)$

The early-time behaviour of this flow is shown in figure 22. At $T^* = 0.04$ one may observe a symmetrical vortex being formed at the tip of the plate. Subsequently this vortex is convected downstream and induces secondary vorticity at the back of the plate. As the plate continues to accelerate, stronger vorticity is shed from the tips of the plate while the initial vortex sheet rolls up (figure 23) to the rear of the plate. Simultaneously diffusion acts to spread both the separating shear layers and the rolled-up vortex sheet so that they eventually coalesce ($T \approx 16$). One may observe then the formation of centres of vorticity along the primary shear layer. As the flow evolves, more centers of vorticity form along the primary shear layer and are convected into the recirculation zone where they dissipate. In figure 24 we compare the results of the present simulations for the length of the recirculating

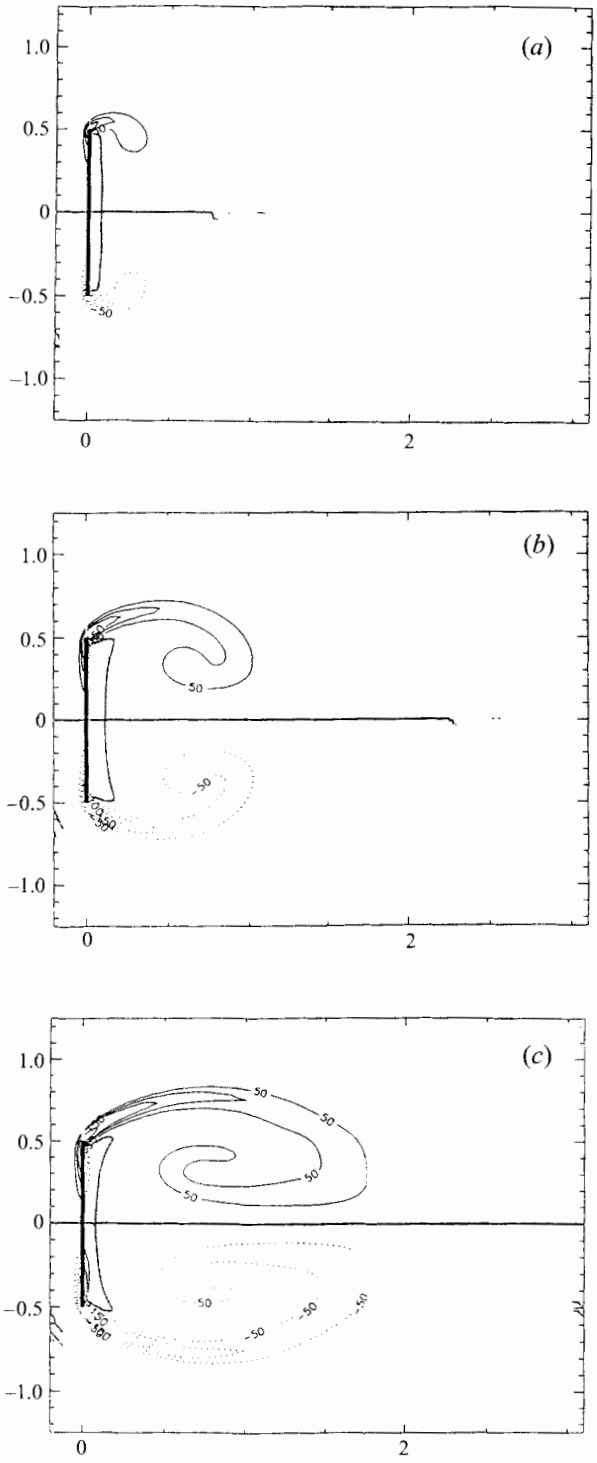

FIGURE 23(*a–c*). For caption see page 208.

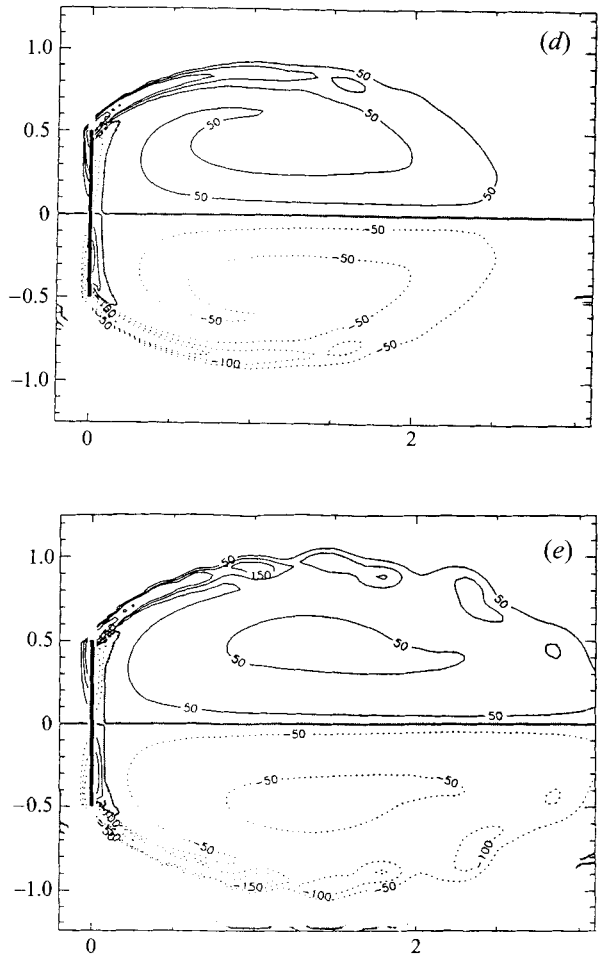

FIGURE 23. Evolution of the vorticity field for an accelerated flat plate ($a = 19.9375$). Vorticity field at $T^* = 1.0, 4.0, 9.0, 16.0, 25.0$ (a–e).

bubble with corresponding experimental results of Taneda & Honji (1971). There is good agreement in the initial stages of the flow that deteriorates with time.

5.2.2. $a = 100 (\alpha = 1.6 \times 10^5)$

As the acceleration of the flow increases one may observe a more rapid development of the vorticity field (figures 25 and 26) than in the previous case. As before, a symmetric vorticity distribution exists around the tips of the plate in the very early stages of the flow. The primary shear layer rolls up faster and induces secondary vorticity the back of the plate at $T \approx 0.16$. However, as the plate accelerates, a new vortex sheet being shed from the plate is already starting to roll up into centres of vorticity at $T \approx 1$. It can be observed in the later pictures of the flow that as the primary vortex layer rolls up and convects away from the high-velocity region of the flow, diffusion acts to spread it out in the recirculation zone. The proximity of this primary vortex to the main shear layer, and its interaction with the secondary vorticity to the back of the plate, seems then to induce a Kelvin–Helmholtz-type instability in the primary shear layer, thus forming discrete centres of vorticity along it. At the same time, as new vortex sheets of higher strength are being formed at the tips of

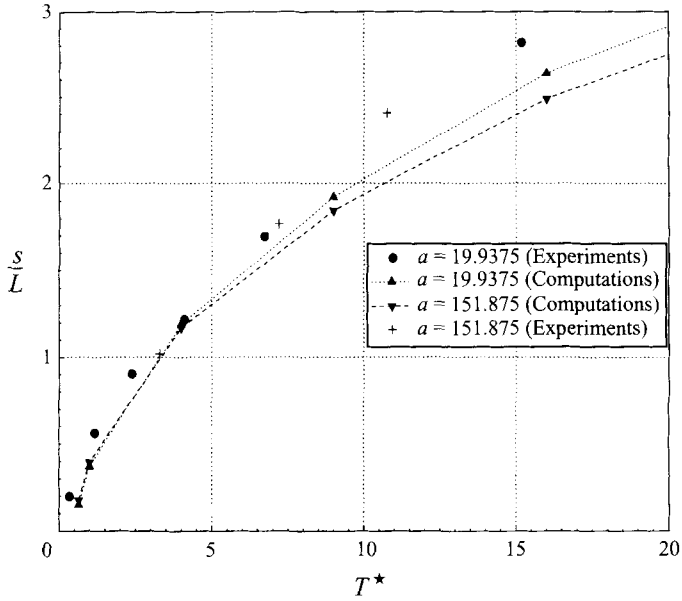

FIGURE 24. Evolution of the wake bubble behind a constantly accelerated flat plate. Comparison with the experimental results of Taneda.

the plate the phenomenon reappears on a different scale. Eventually then centres on vorticity appear all along the shear layer. We stopped the simulations for this flow at $T^\star \approx 25$ when roundoff errors accumulated, thus inducing asymmetry in the flow. The streamlines of the flow are presented in figure 27. One may observe slight undulations along the separating streamline and a region of relatively low velocity in the recirculating zone of the plate. Compared to the contours of the vorticity field the instantaneous streamlines exhibit a milder variation. This could possibly challenge experimental works that deduce the vorticity of the flow from the instantaneous streaklines using techniques such as particle image velocimetry.

5.2.3. $a = 151.875 (\alpha = 2.43 \times 10^5)$

In figures 28 and 29 we present the evolution of the vorticity field of this flow. The evolution of the flow is quite similar to the $a = 100$ case. One may observe however that the centres of vorticity remain on the periphery of the recirculating zone longer, while a large low-vorticity region is formed in the centre. In figure 24 we compare the length of the recirculating bubble as computed by the present simulations with the experiments of Taneda & Honji (1971). Again good agreement is observed for earlier times while the results deviate for later times.

5.2.4. $a = 415 (\alpha = 6.64 \times 10^5)$

As the acceleration is increased the primary vortex becomes stronger and forms closer to the plate (figure 30). This has as a result the formation of centres of vorticity along the separating shear layers near the tips of the plate. One may observe a dense array of discrete centres of vorticity springing off the tips of the plate even at earlier times. Further from the tips of the plate the distance between the centres of vorticity grows larger. This change in the wavelength may be explained by examining the source of the straining flow that triggers the Kelvin–Helmholtz-type instability. Near the tips of the plate vorticity of opposite sign is extracted from the back of the plate.

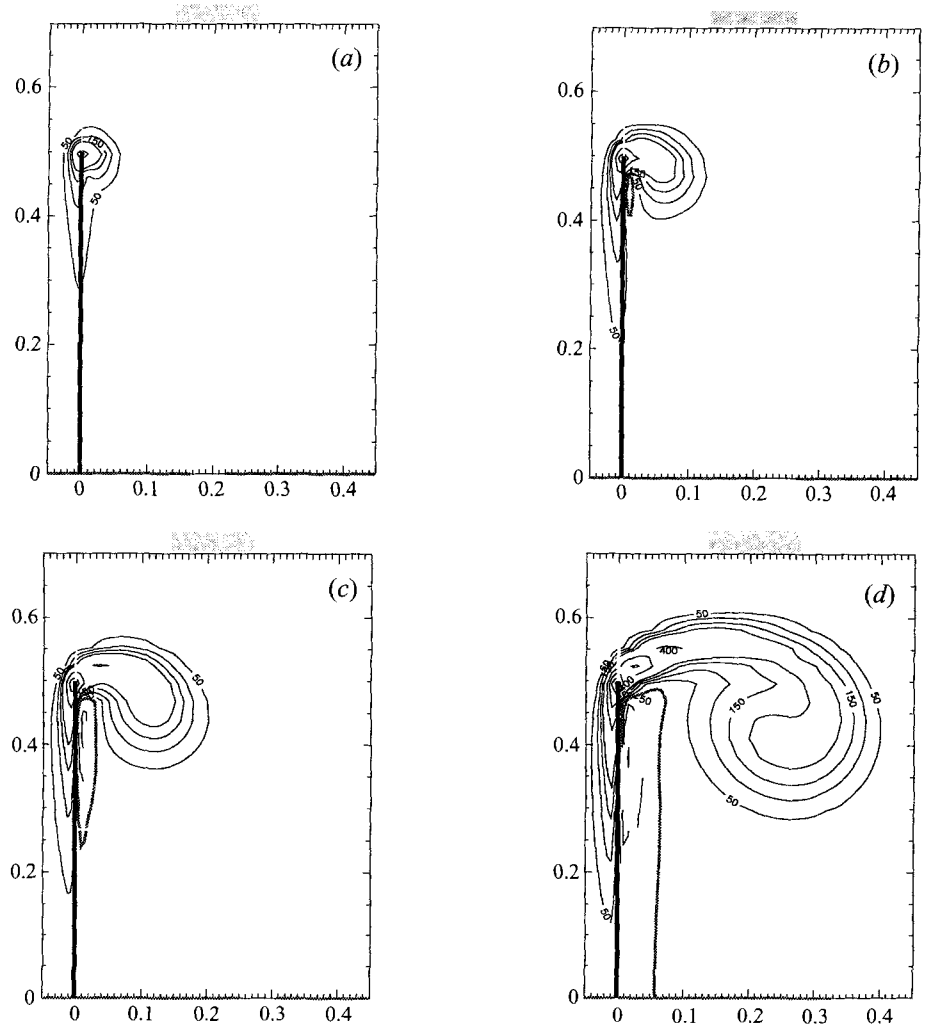

FIGURE 25. Early time evolution of the vorticity field for an accelerated flat plate ($a = 100$). Vorticity field at $T^* = 0.04, 0.16, 0.36, 0.64$ (a–d).

Hence there is a higher velocity difference along the sides of the separating shear layer near the plate tips than there is further away. Moreover the shear layer that is formed near the tips of the plate has not been affected significantly by diffusion hence it is stronger and shorter than the respective vortex sheet downstream. This implies shorter wavelength Kelvin–Helmholtz waves being triggered by the straining flow. As vortices travel downstream (figure 31) diffusion acts to reduce their strength so that they have a weaker influence on the shear layer. Moreover the shear layer has been thickened by the effects of viscosity resulting in longer unstable wavelengths. Note the similarity exhibited by the instantaneous streamlines of the flow (figure 32) with the respective streamlines for $a = 100$ (figure 27).

5.2.5. $a = 1050\,(\alpha = 16.8 \times 10^5)$

This is the highest rate of acceleration considered for the flat plate and is by far the most interesting one. The breaking of the vortex sheet into distinct vortices is even more pronounced in this case. In figure 33 one may observe the early-time behaviour

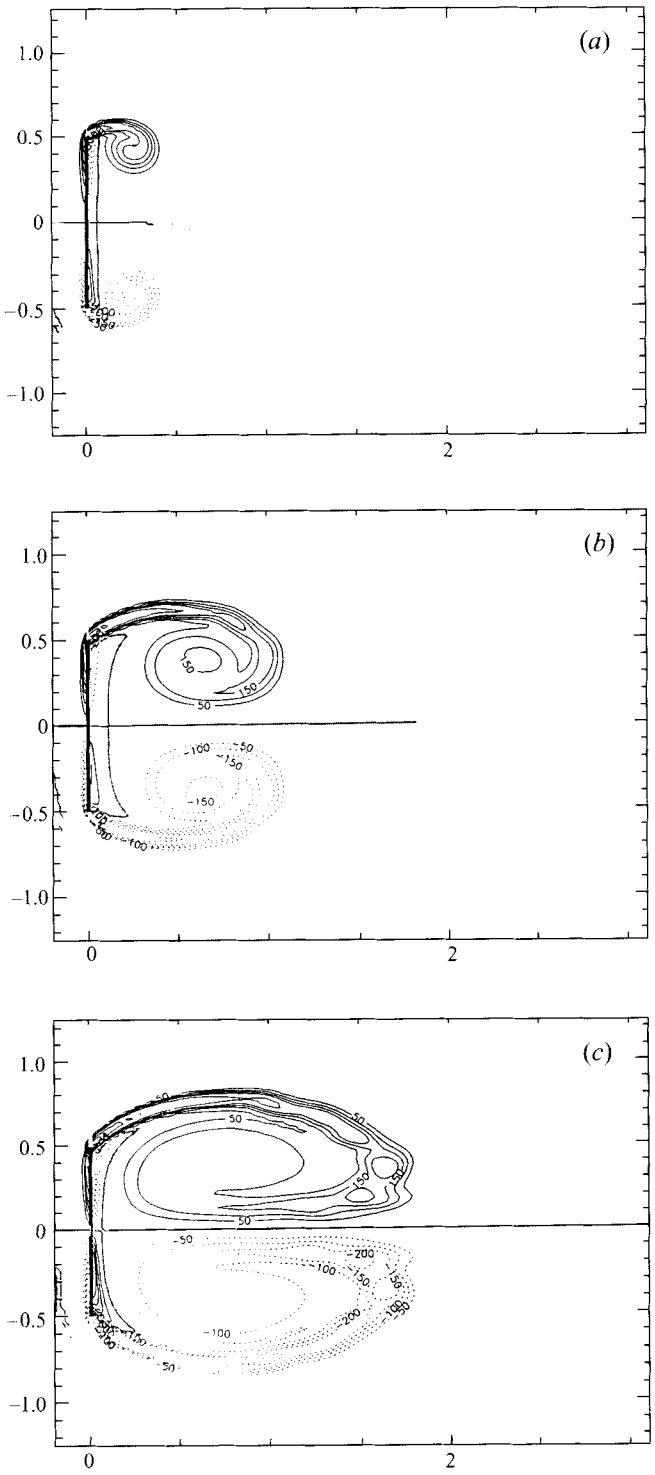

FIGURE 26(*a–c*). For caption see page 212.

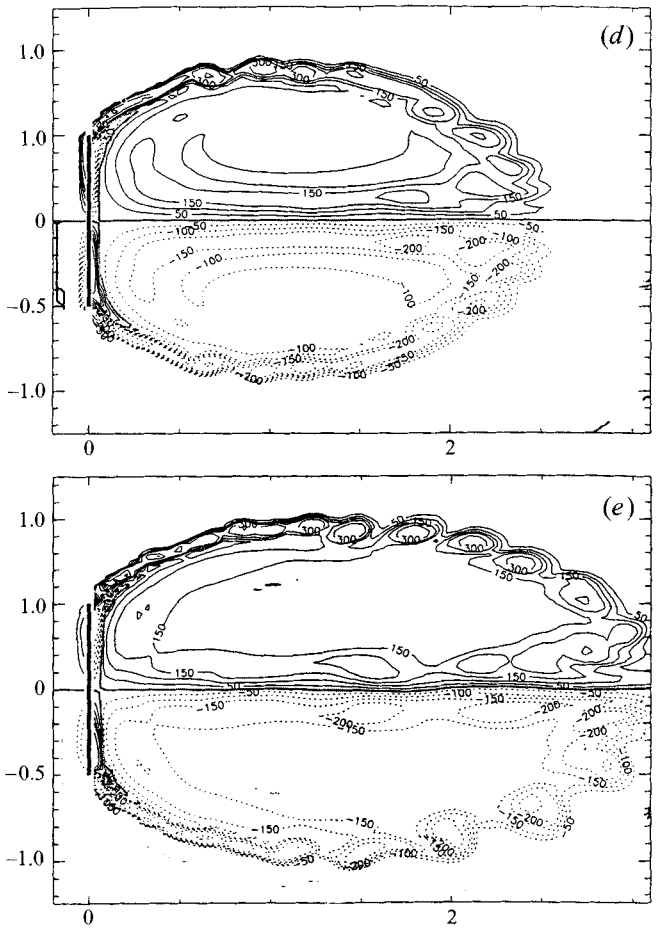

FIGURE 26. Evolution of the vorticity field for an accelerated flat plate ($a = 100$). Vorticity field at $T^* = 1.0, 4.0, 9.0, 16.0, 25.0$ (a–e).

of the flow. A strong primary vortex forms on the back of the plate inducing a strong secondary vorticity region. One may observe the immediate breakup of the shear layer ($T^* = 0.36$) and at the same time the process of shedding discrete vortices from the tips of the plate. Thin, strong shear layers are formed at the tips of the plate that are subjected to a Kelvin–Helmholtz-type instability. In figure 34 we observe the evolution of the flow at later times. Further away from the tips of the plate larger wavelengths are observed as the shear layer is thicker and the destabilizing strain flow is of smaller magnitude. Stronger variations are exhibited by the streamlines of the flow (figure 35) giving vorticity rolls along the primary shear layer. As evidence for the accuracy of our simulations note that the flow remained symmetric for all the times presented herein, although no symmetry constraint was imposed on our calculations.

5.3. *Drag forces; bubble length*

Uniformly accelerated flows have been known to exhibit similarity when time is scaled as in (44). This similarity was first studied experimentally by Noca (1990). He presented streaklines behind flat plates at a 45° angle of attack, exhibiting remarkable similarity of the flow at corresponding instances of time.

For the flat plate normal to the flow, the results of the simulations demonstrate

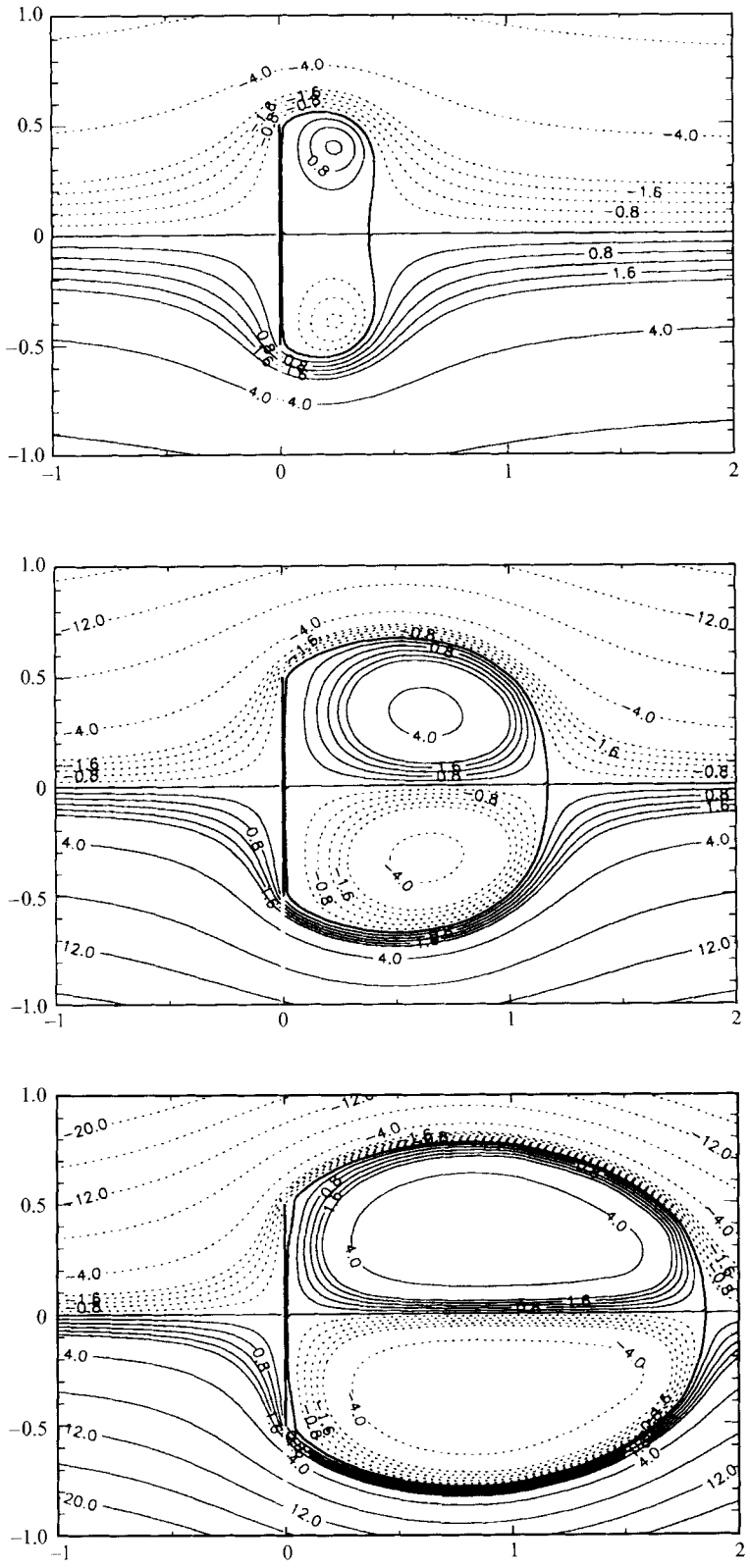

FIGURE 27. Evolution of the streamlines for an accelerated flat plate ($a = 100$).

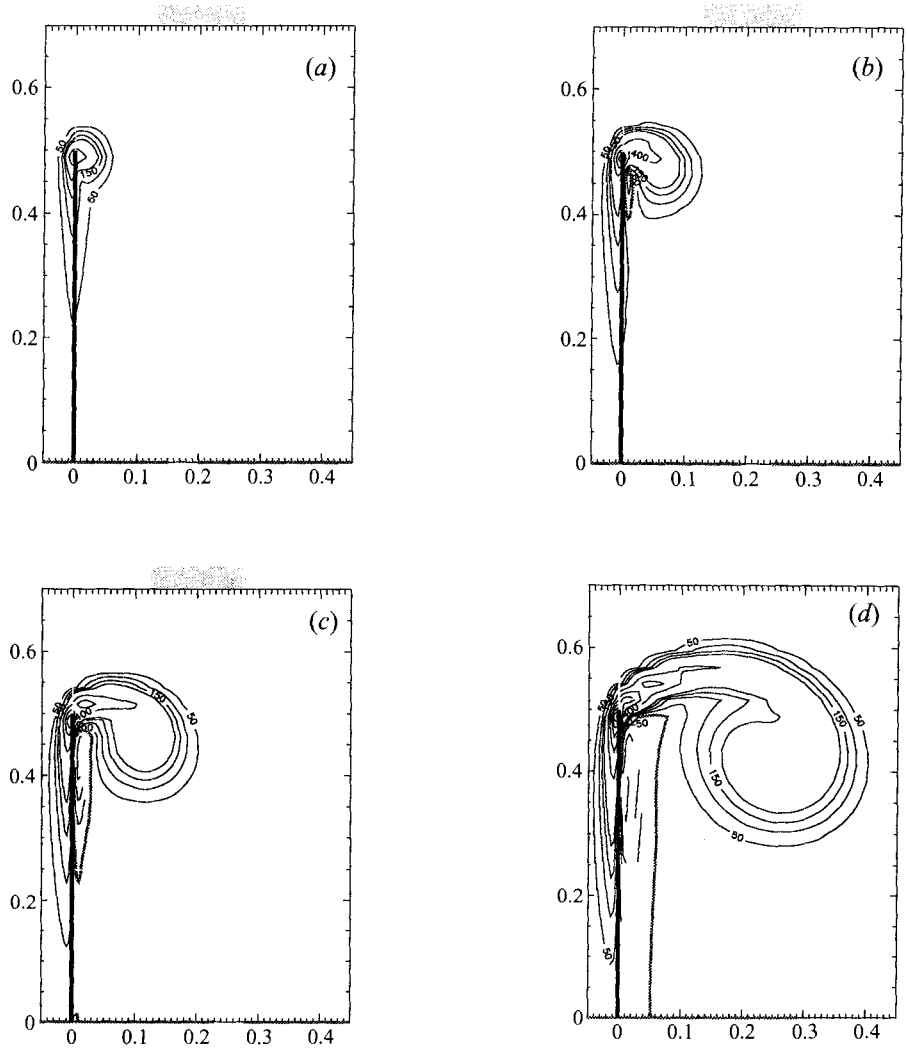

FIGURE 28. Early time evolution of the vorticity field for an accelerated flat plate ($a = 151.875$). Vorticity field at $T^* = 0.04, 0.16, 0.36, 0.64$ (a–d).

and quantify this flow similarity. In figures 36 and 37 we present the evolution of the length of the recirculating bubble and the drag coefficient of the plate for the above studied accelerations. Our results on the length of the recirculating bubble seem to collapse to a single curve, independent of the rate of acceleration. Note however that the present computations do not seem to coincide with the power law proposed by Taneda & Honji (1971).

A striking collapse of the data is observed for the drag coefficient of the flow. The drag coefficient as normalized in (45) is independent of the acceleration of the flow (especially for earlier times). This may be attributed to the inviscid development of the flow and the similarity in the formation of the vortical centres along the separating shear layers. Moreover, the data collapse demonstrates the consistency of the present simulations and implies that T^* is the 'correct' non-dimensional time and the computed C_d the 'correct' drag coefficient.

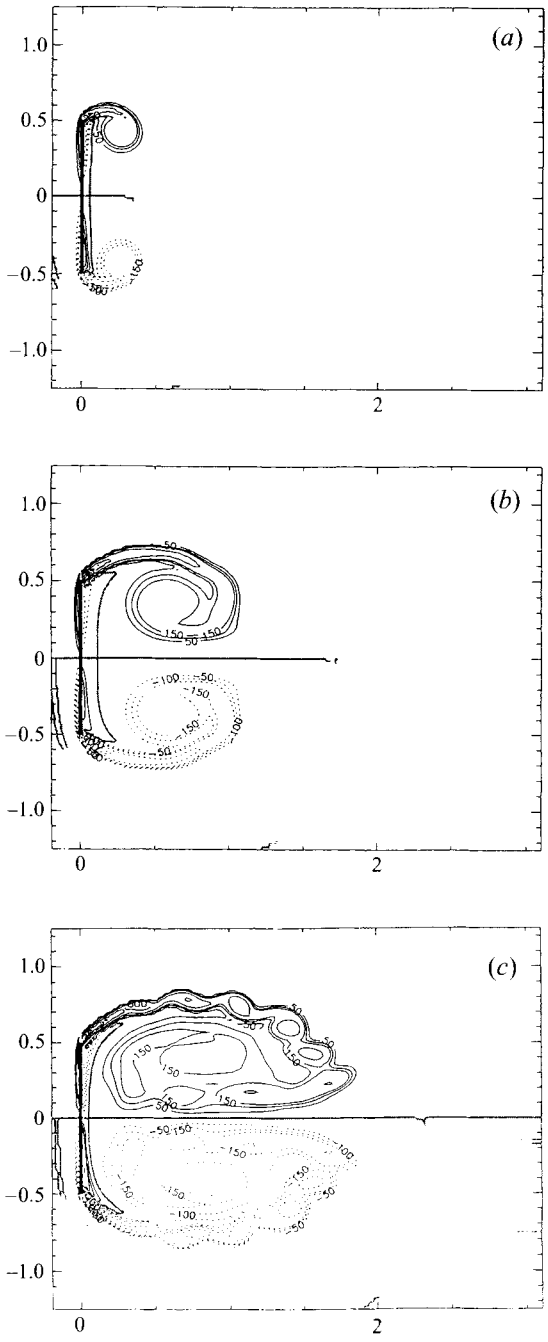

FIGURE 29(*a–c*). For caption see page 216.

5.4. *Discussion*

Our simulations of a uniformly accelerating plate reveal the systematic development of small centres of vorticity along the large-scale primary vortex sheets. Such vortices have been observed (figure 38) in related experimental works (Pierce 1961; Pullin & Perry 1980; Lian & Huang 1989). In a related flow Tsai & Yue (1993) observed the

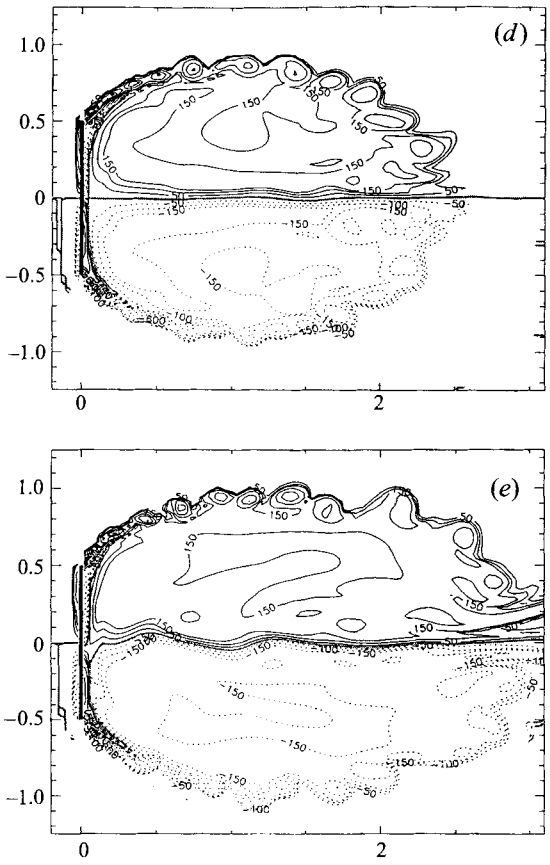

FIGURE 29. Evolution of the vorticity field for an accelerated flat plate ($a = 151.875$). Vorticity field at $T^* = 1.0, 4.0, 9.0, 16.0, 25.0$ (a–e).

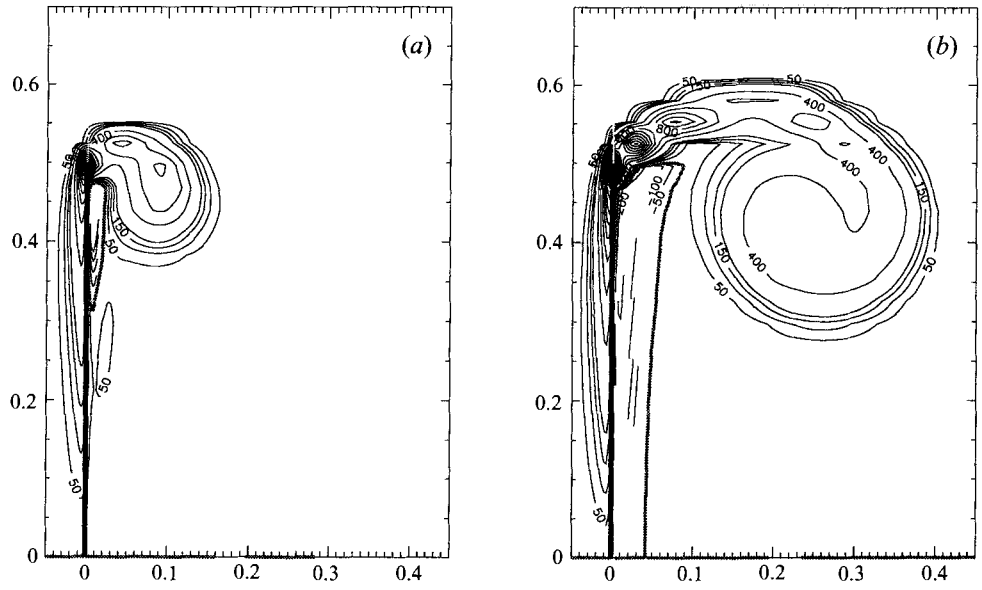

FIGURE 30. Early time evolution of the vorticity field for an accelerated flat plate ($a = 415$). Vorticity field at $T^* = 0.04, 0.16$ (a,b).

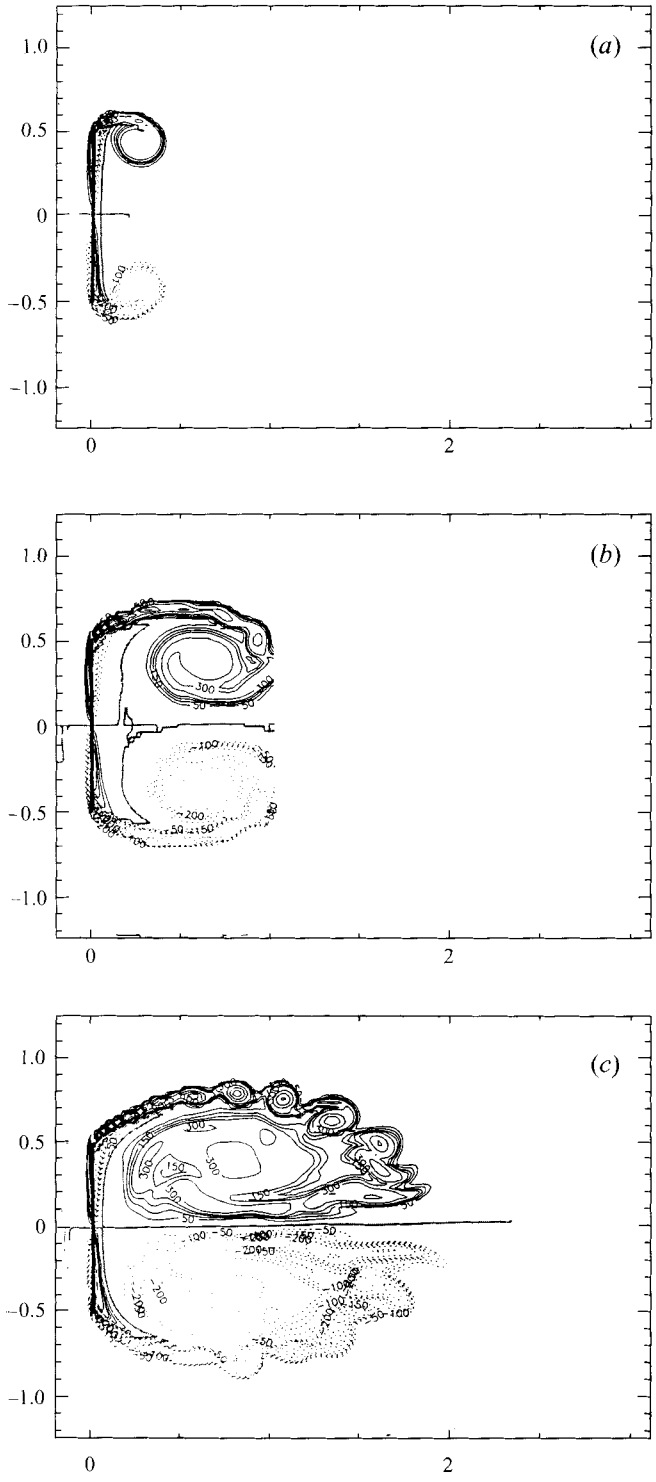

FIGURE 31. Evolution of the vorticity field for an accelerated flat plate ($a = 415$). Vorticity field at $T^* = 1.0, 4.0, 9.0$ (a–c).

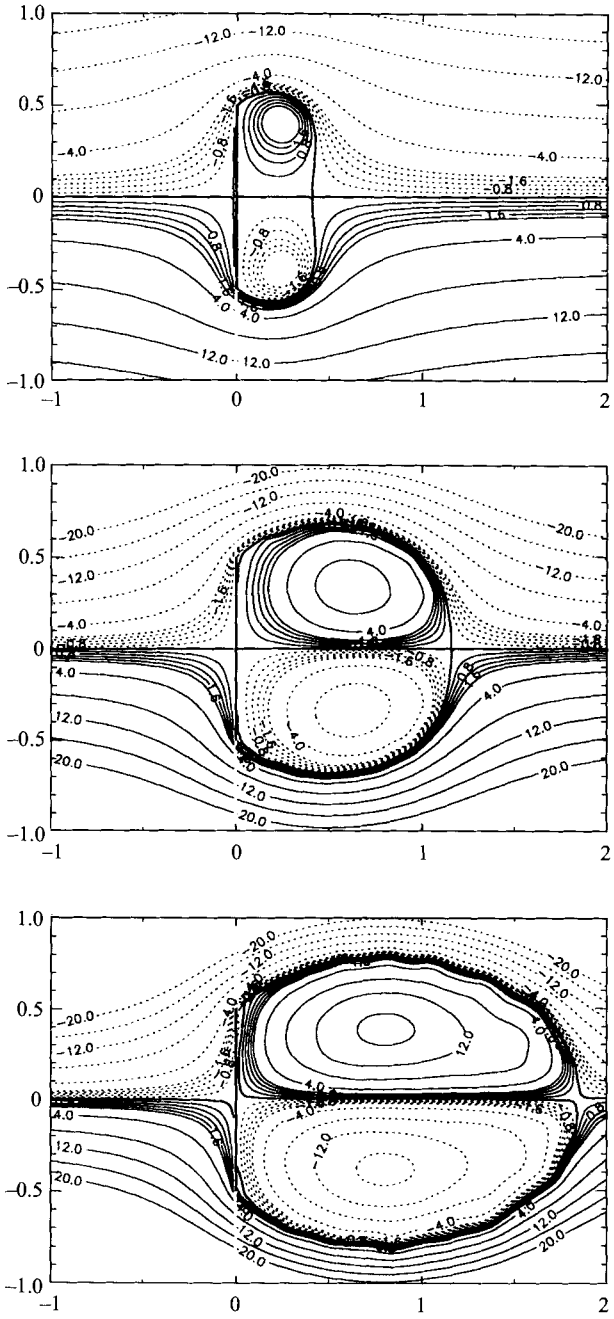

FIGURE 32. Evolution of the streamlines for an accelerated flat plate ($a = 415$).

formation of discrete centres of vorticity in the separating shear layer of a flat plate due to its interaction with a free surface. However, there is a debate as to whether this vortex formation is due to an inherent instability of the flow or to perturbations caused by the experimental apparatus. Pierce (1961) and Lian & Huang (1989) support the instability idea while Pullin & Perry (1980) interpret this behaviour as an apparatus-induced neutrally perturbed flow. The stability of an evolving two-dimensional sheet

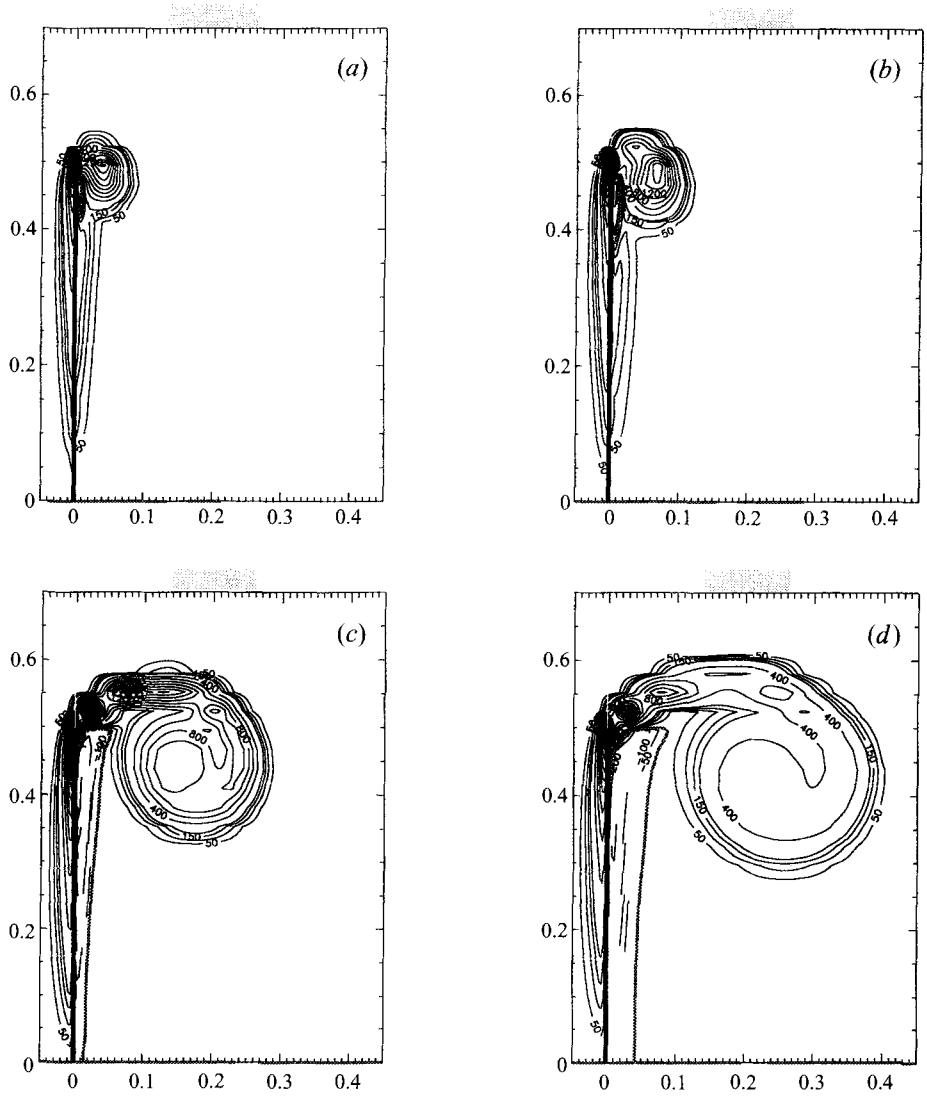

FIGURE 33. Early time evolution of the vorticity field for an accelerated flat plate ($a = 1050$). Vorticity field at $T^* = 0.04, 0.16, 0.36, 0.64$ (a–d).

has also been studied theoretically by Moore (1976). He applied his theory to a tightly wound, time-decaying, spiral vortex sheet that he showed to be stable.

In the present direct numerical simulations, perturbations may be introduced due to numerical errors. As no symmetry is imposed in our simulations, experience dictates that roundoff errors would manifest themselves by triggering an asymmetry to the flow. Indeed, such behaviour is observed at long times and higher accelerations. Also, the developing shear layers of our simulations increase in strength with time whereas Moore's analysis deals with a tightly wound spiral vortex sheet whose strength decreases with time. Note that Moore's model is more related to the vortex sheet roll-up observed behind an impulsively started plate, for which indeed no instability was observed.

We believe then that the formation of the vortex centres along the separating

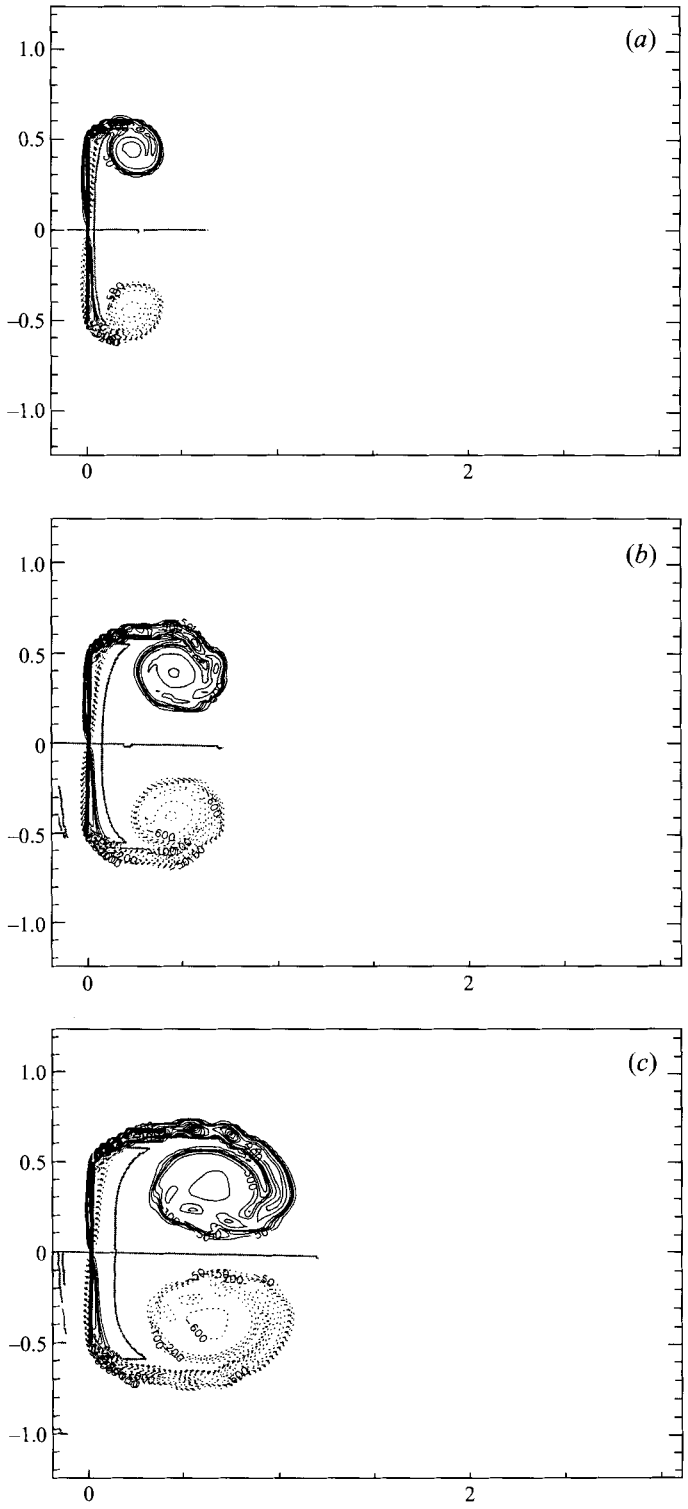

FIGURE 34(*a–c*). For caption see facing page.

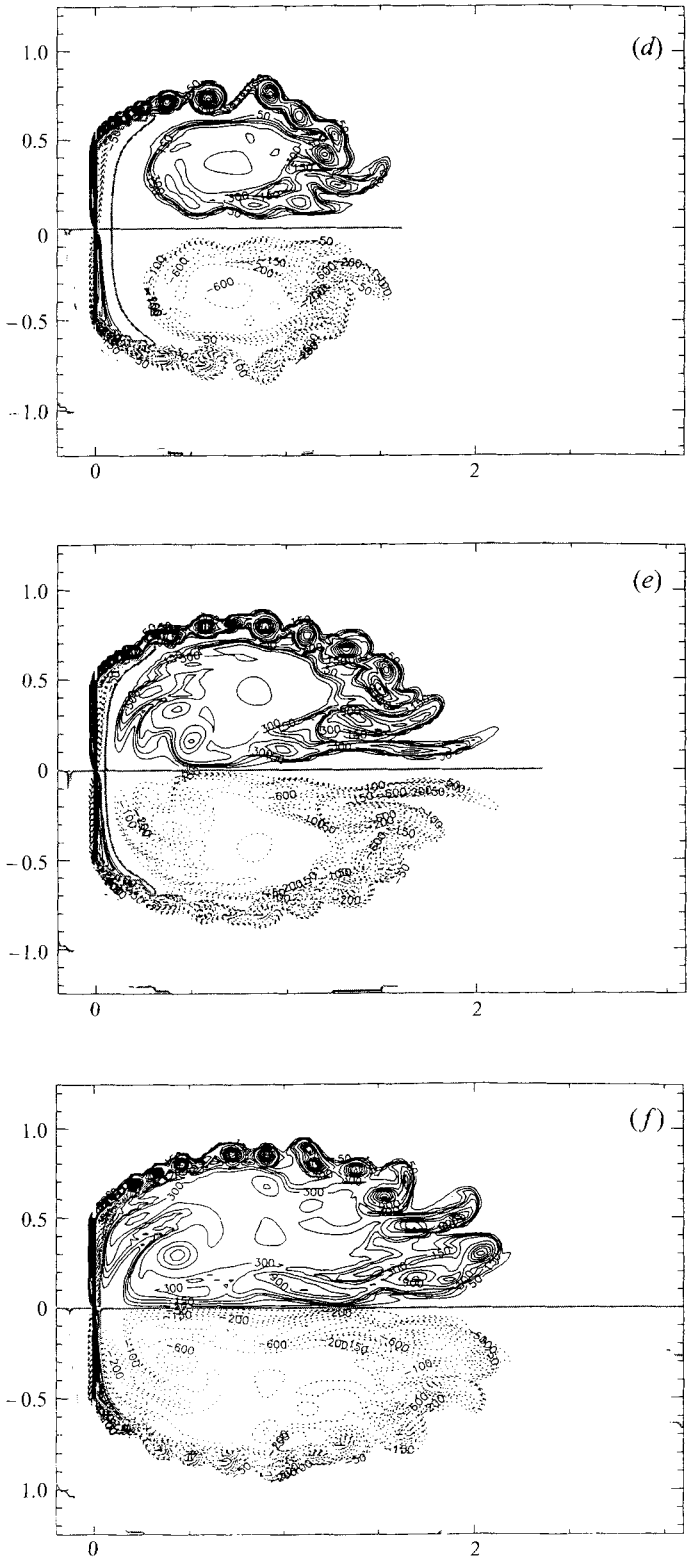

FIGURE 34. Evolution of the vorticity field for an accelerated flat plate ($a = 1050$). Vorticity field at $T^* = 1.0, 2.25, 4.0, 6.25, 9.0, 12.25$ (*a–f*).

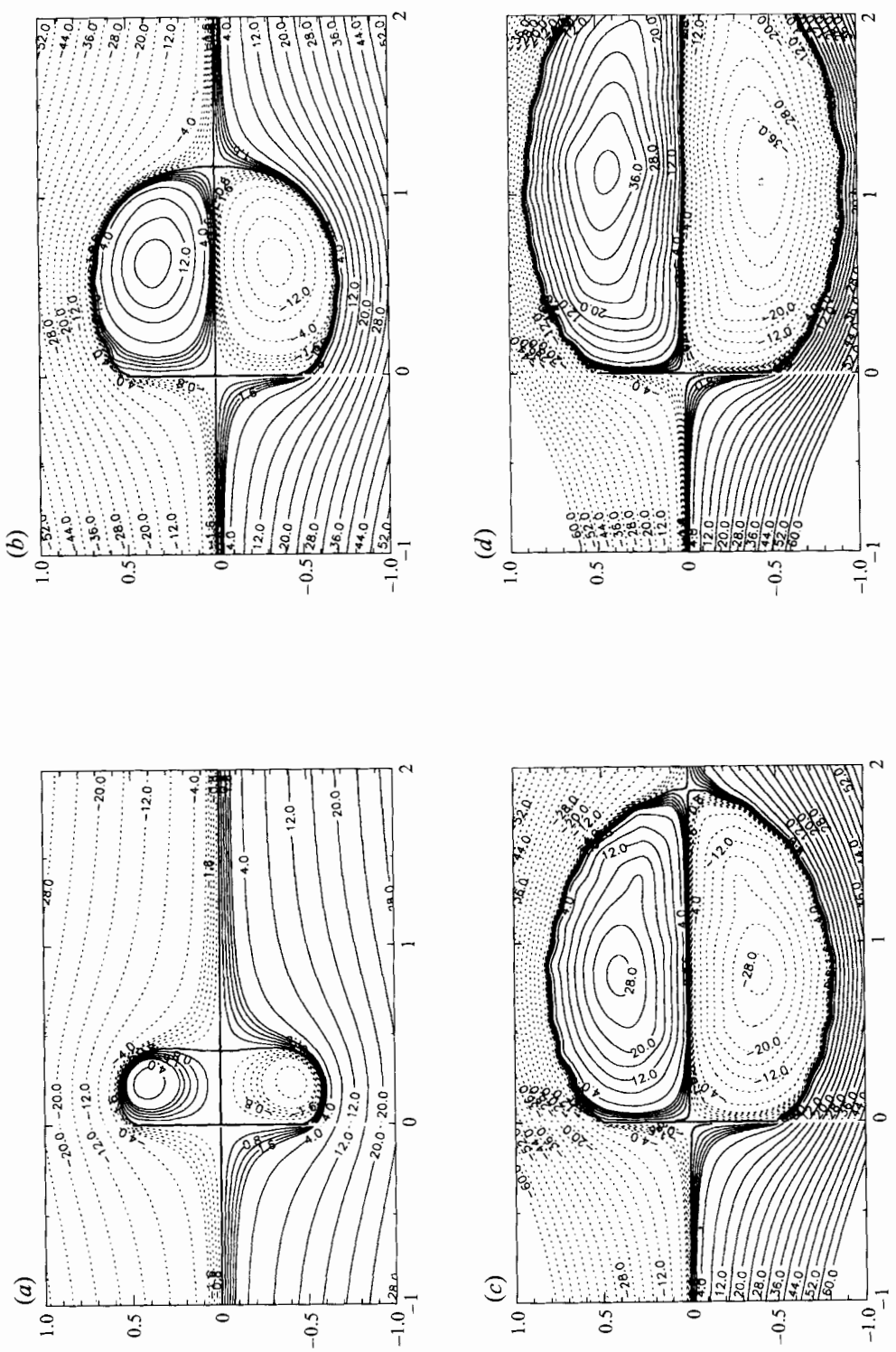

FIGURE 35. Evolution of the streamlines for an accelerated flat plate ($a = 1050$) Streamlines at : $T^* = 1.0$, 4.0, 9.0, 12.25 (a–d).

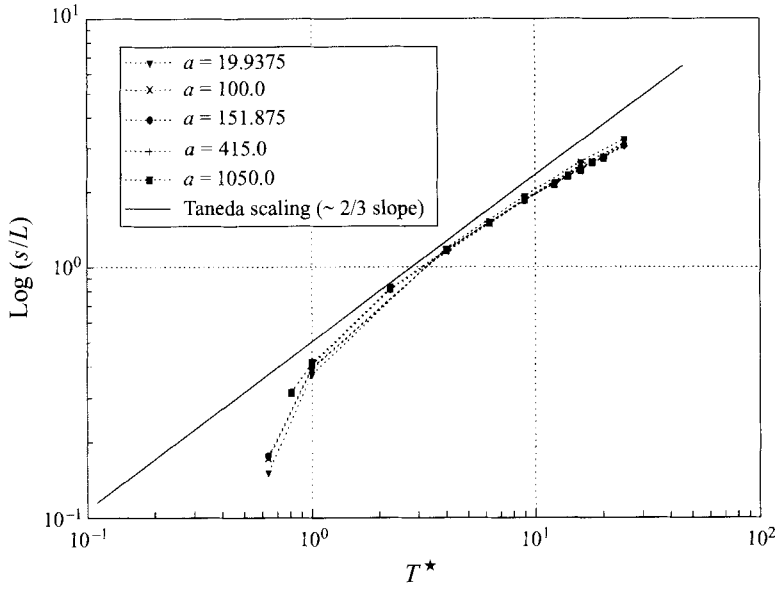

FIGURE 36. Evolution of the wake bubble behind a constantly accelerated flat plate. Comparison with the scaling of Taneda.

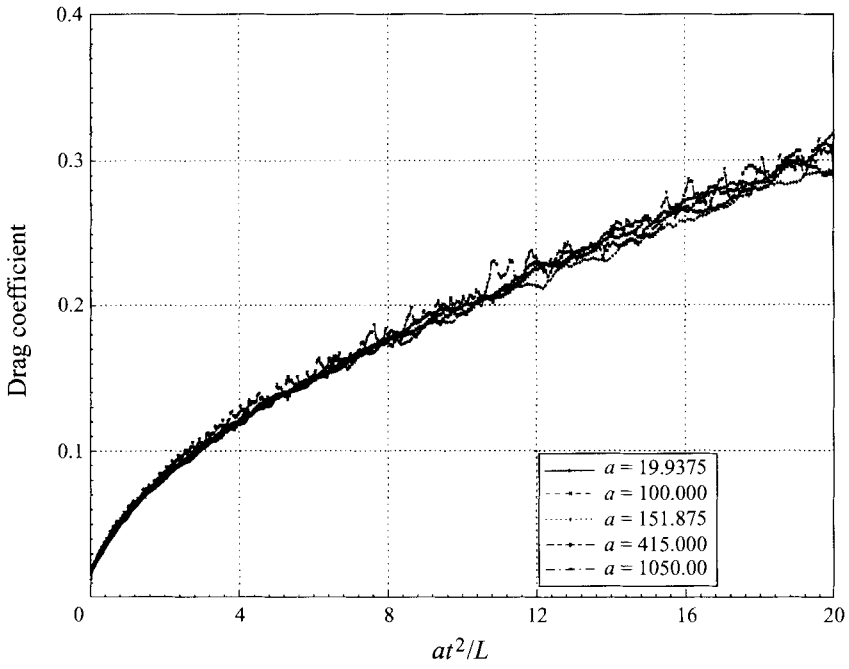

FIGURE 37. Evolution of the scaled drag coefficient for a constantly accelerated flat plate.

(a)

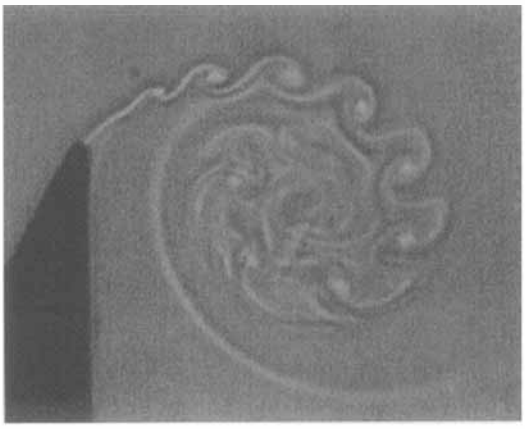

(b)

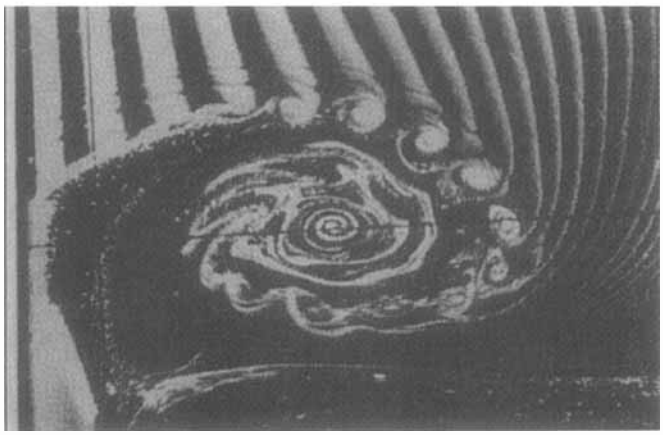

(c)

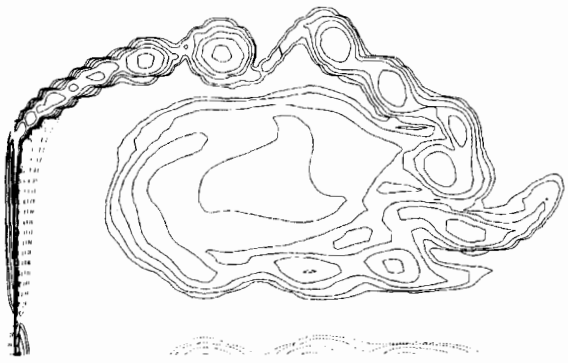

FIGURE 38. Photographic evidence of the shear layer instability, for a uniformly accelerated bluff body flows. (*a*) Flow past a uniformly accelerating wedge with $\alpha = 2.06 \times 10^9$ at $T^* = 3.0$ (Pierce 1961). (*b*) Flow past a uniformly accelearting plate with $\alpha = 24.51 \times 10^6$ at $T^* = 4.37$ (Lian & Huang 1989) (*c*) Present computations for $\alpha = 1.68 \times 10^6$ at $T^* = 6.25$.

shear layer is an intrinsic behaviour of the flow due to a Kelvin–Helmholtz-type instability. The wavelength and the location of the onset of this instability depend on the strength of the vortex sheet, its variable thickness (due to diffusion) and the variable shear across it (due to the continuous acceleration, the secondary vorticity and the primary vortex roll-up). The instability along the primary shear layer is also driven by the interaction of the primary and secondary vorticity at the tips of the plate. This interaction has an oscillating character that induces perturbations to excite the various modes of the observed Kelvin–Helmholtz instabilities. A confirmation of the inviscid evolution of the flow along the separating layers is provided by the scaling of the drag coefficient and the length of the recirculating bubble.

6. Conclusions

We have presented a computational study of the unsteady flow behind a zero-thickness flat plate started impulsively or uniformly accelerated normal to the flow.

For the impulsively started plate the present results complement related experimental works, while providing quantities such as the vorticity of the flow field and the forces experienced by the body. The development of the flow is similar for all the Reynolds numbers that were simulated. The separating shear layer rolls up into a vortex in the lee of the plate, inducing initially a region of secondary vorticity. Diffusion acts to increase the width of the shear layer and reduce the strength of the vortex, resulting in a stable configuration.

A different behaviour is observed for the separating shear layer of a uniformly accelerated plate. The continuous increase of the shear flow overcomes the effects of diffusion, increasing the strength of the separating shear layer and inducing a Kelvin–Helmholtz-type instability. The wavelength and the onset of this instability depend on the acceleration of the plate. The present simulations are the first to confirm related experimental evidence on the formation of vortex centres along the separating shear layers of an accelerating flat plate. Such undulations have been attributed to experimental defects, but the present simulations suggest that this is an intrinsic behaviour of the flow. Finally, the drag coefficient of the plate is shown to scale due to the similarity in the inviscid development of the flow.

We wish to acknowledge many extensive and enlightening discussions with Professor Anthony Leonard. We are indebted to Mr Mark Brady (GALCIT) for his help throughout the completion of this work. One of us (P.K.) benefited considerably from several informal discussions with Dr Nagi Mansour and Dr Kareem Shariff of NASA Ames. We also wish to thank Professor Madeleine Coutanceau for kindly providing us with original pictures from her related experimental work. Computer time was provided by NASA Ames and Caltech's Jet Propulsion Laboratory Supercomputing Project.

REFERENCES

ANTON, L. 1939 Formation of a vortex at the edge of a plate. *Ing. Arch.* **10**, 411.

BARNES, J. E. & HUT P. 1986 A hierarchical $\mathcal{O}$(N logN) force-calculation algorithm. *Nature* **324**, 446–449.

BATCHELOR, G. K. 1967 *An Introduction to Fluid Dynamics.* Cambridge University Press.

BEALE, J. T. 1986 On the accuracy of vortex methods at large times. *Proc. Workshop on Comp. Fluid Dyn. and React. Gas Flows IMA, Univ. of Minnesota.*

CHORIN, A. J. 1973 Numerical study of slightly viscous flow. *J. Fluid Mech.* **57**, 380–392.

CHUA, K. 1990 Vortex simulation of separated flows in two and three dimensions. PhD Thesis California Institute of Technology.

COUTANCEAU, M. & BOUARD, R. 1977 Experimental determination of the main features of the viscous flow in the wake of a circular cylinder in uniform translation. Part 2: Unsteady flow. *J. Fluid Mech.* **79**, 257–272.

DEGOND, P. & MAS-GALLIC, S. 1989 The weighted particle method for convection – diffusion equations, Part I : The case of an isotropic viscosity, Part II : The anisotropic case. *Math. Comput.* **53**, 485–526.

DENNIS, S. C. R., QIANG, W., COUTANCEAU, M. & LAUNAY, J-L. 1993 Viscous flow normal to a flat plate at moderate Reynolds numbers. *J. Fluid Mech.* **248**, 605–635.

FORNBERG, B. 1980 A numerical study of steady viscous flow past a circular cylinder. *J. Fluid Mech.* **98**, 819–855.

GREENGARD, L. & ROHKLIN, V. 1987 A fast algorithm for particle simulations. *J. Comput. Phys.* **73**, 325–348.

HUDSON, J. D. & DENNIS, S. C. R. 1985 The flow of a viscous incompressible fluid past a normal flat plate at low and intermidiate Reynolds numbers: the wake. *J. Fluid Mech.* **160**, 369–383.

IN, K. M., CHOI, D. H. & KIM, M. U. 1995 2-dimensional viscous flow past a flat plate. *Fluid Dyn. Res.* **15**, 13–24.

INGHAM, T. B., TANG, T. & MORTON, B. R. 1991 Steady two-dimensional flow past a normal flat plate. *Z. Agnew. Math. Phys.* **42**, 584–604 (referred to herein as ITM).

KOUMOUTSAKOS, P. 1993 Direct numerical simulations of unsteady separated flows using vortex methods. PhD Thesis, California Institute of Technology.

KOUMOUTSAKOS, P. 1996 Inviscid axisymmetrization of an elliptical vortex. *submitted.*

KOUMOUTSAKOS, P. & LEONARD, A. 1995 High Resolution simulations of the flow around an impulsively started cylinder using vortex methods. *J. Fluid Mech.* **296**, 1–38.

KOUMOUTSAKOS, P., LEONARD, A. & PEPIN, F. 1994 Boundary conditions for viscous vortex methods. *J. Comput. Phys.* **113**, 52–61 (referred to herein as KLP).

KRASNY, R. 1991 Vortex sheet computations : roll-up, wakes, separation. *Lect. Appl. Maths* **28**, 385.

LAVAL, H. & QUARTAPELLE, L. 1990 A fractional step Taylor-Galerkin method for unsteady incompressible flows. *Intl J. Numer. Meth. Fluids*, **11**, 501.

LEONARD, A. 1980 Vortex methods for flow simulation. *J. Comput. Phys.* **37**, 289–335.

LIAN, Q. X. & HUANG, Z. 1989 Starting flow and structures of the starting vortex behind bluff bodies with sharp edges. *Exps. Fluids* **8**, 95.

LIGHTHILL, M. J. 1963 Introduction. In *Boundary Layer Theory* (ed. J. Rosenhead), pp. 54–61. Oxford University Press,

MESSITER, A. F. 1970 Boundary layer flow near the trailing edge of a flat plate. *SIAM J. Appl. Maths* **18**, 241–257.

MOORE, D. W. 1976 The stability of an evolving two-dimensional vortex sheet. *Mathematika* **23**, 35.

NAJJAR, R. M. & VANKA, A. P. 1995 Simulations of the unsteady separated flow past a normal flat plate. *Intl J. Numer. Meth. Fluids* **21**, 525–547.

NATARAJAN, R., FORNBERG, B. & ACRIVOS, A. 1993 Flow past a row of flat plates at large Reynolds numbers. *Proc. R. Soc. Lond.* A441, 211–235.

NOCA, F. 1990 Flow similarity for uniformly accelerated motions. *Ae200-Research Report*, California Institute of Technology.

PEPIN, F. 1990 Simulation of the flow past an impulsively started cylinder using a discrete vortex method. PhD Thesis, California Institute of Technology.

PIERCE, D. 1961 Photographic evidence of the formation and growth of vorticity behind plates accelerated from rest in still air. *J. Fluid Mech.* **11**, 460–464.

PRANDTL, L. 1904 Über Flüssigkeitsbewegung bei sehr kleiner Reibung. *Verhandlungen des III. Internationalen Mathematiker-Kongresses,Heidelberg, 1904*, pp. 484–491. Leipzig: B. G. Teubner, 1905.

PULLIN, D. & PERRY, A. E. 1980 Some flow visualization experiments on the starting vortex. *J. Fluid Mech.* **88**, 239–255.

SARPKAYA, T. 1975 An inviscid model of two-dimensional vortex shedding for transient and asymptotically steady separated flow over an inclined plate. *J. Fluid Mech.* **68**, 109–128.

SCHMALL, R. A. & KINNEY, R. B. 1974 Numerical study of unsteady viscous flow past a lifting plate. *AIAA J.* **12**, 1566.

SCHOENBERG, I. J. 1973 *Cardinal Spline Interpolation.* SIAM, Philadelphia.

STEWARTSON, K. 1974 Multistructured boundary layers on flat plates and related bodies. *Adv. Appl. Mech.* **14**, 146–239.

TAMADDON-JAHROMI, H. R., TOWNSEND, P. & WEBSTER, M. F. 1994 Unsteady viscous flow past a flat plate orthogonal to the flow. *Comput. Fluids* **23**, 433.

TANEDA, S. & HONJI, H. 1971 Unsteady flow past a flat plate normal to the direction of motion. *J. Phys. Soc. Japan* **30**, 262.

TSAI, W-T. & YUE, D. K. P. 1993 Interactions between a free surface and a vortex sheet shed in the wake of a surface piercing plate. *J. Fluid Mech.* **257**, 691–721.

VILLAT, H. 1930 *Lecons sur la Theorie des Tourbillons.* Gauthiers-Villars.

WEDEMEYER, X. 1961 Ausbildung eines wirbelpaares an den kanten einer platte. *Max-Planck Institut für Ströungsforschung, Bericht.* 56-B-06.

YOSHIDA, Y. & NOMURA, T. 1985 A transient solution method for the finite element incompressible Navier–Stokes equations. *Intl J. Numer. Meth. Fluids* **5**, 873.